Arctic Ocean CO_2 uptake: an improved multi-year estimate of the air–sea CO_2 flux incorporating chlorophyll-a concentrations

Sayaka Yasunaka[1,2], Eko Siswanto[1], Are Olsen[3], Mario Hoppema[4], Eiji Watanabe[2], Agneta Fransson[5], Melissa Chierici[6], Akihiko Murata[1,2], Siv K. Lauvset[3,7], Rik Wanninkhof[8], Taro Takahashi[9], Naohiro Kosugi[10], Abdirahman M. Omar[7], Steven van Heuven[11], and Jeremy T. Mathis[12]

[1]Research and Development Center for Global Change, Japan Agency for Marine-Earth Science and Technology, Yokosuka, Japan

[2]Institute of Arctic Climate and Environment Research, Japan Agency for Marine-Earth Science and Technology, Yokosuka, Japan

[3]Geophysical Institute, University of Bergen and Bjerknes Centre for Climate Research, Bergen, Norway

[4]Alfred Wegener Institute Helmholtz Centre for Polar and Marine Research, Climate Sciences Department, Bremerhaven, Germany

[5]Norwegian Polar Institute, Fram Centre, Norway

[6]Institute of Marine Research, Tromsø, Norway

[7]Uni Research Climate, Bjerknes Centre for Climate Research, Bergen, Norway

[8] National Oceanic and Atmospheric Administration, Atlantic Oceanographic and Meteorological Laboratory, Miami, FL, USA

[9]Lamont-Doherty Earth Observatory of Columbia University, Palisades, NY, USA

[10]Oceanography and Geochemistry Research Department, Meteorological Research Institute, Japan Meteorological Agency, Tsukuba, Japan

[11]Energy and Sustainability Research Institute Groningen, Groningen University, The Netherlands

[12] National Oceanic and Atmospheric Administration, Arctic Research Program, Seattle, WA, USA

Abstract

We estimated monthly air–sea CO_2 fluxes in the Arctic Ocean and its adjacent seas north of 60° N from 1997 to 2014. This was done by mapping partial pressure of CO_2 in the surface water (pCO_{2w}) using a self-organizing map (SOM) technique incorporating chlorophyll-a concentration (Chl-a), sea surface temperature, sea surface salinity, sea ice concentration, atmospheric CO_2 mixing ratio, and geographical position. We applied new algorithms for extracting Chl-a from satellite remote sensing reflectance with close

examination of uncertainty of the obtained Chl-a values. The overall relationship between pCO_{2w} and Chl-a was negative, whereas the relationship varied among seasons and regions. The addition of Chl-a as a parameter in the SOM process enabled us to improve the estimate of pCO_{2w} particularly via better representation of its decline in spring which resulted from biologically mediated pCO_{2w} reduction. As a result of the inclusion of Chl-a, the uncertainty in the CO_2 flux estimate was reduced, with a net annual Arctic Ocean CO_2 uptake of 180 ± 130 TgC y^{-1}. Seasonal to interannual variation of the CO_2 influx was also figured out.

1. Introduction

The Arctic Ocean and its adjacent seas (Fig. 1) generally act as a sink for atmospheric CO_2 because of the high solubility of CO_2 in their low-temperature waters, combined with extensive primary production during the summer season (Bates and Mathis, 2009). The Arctic Ocean and its adjacent seas consist of complicated subregions that include continental shelves, central basins, and sea-ice-covered areas. Therefore, the surface partial pressure of CO_2 (pCO_{2w}) distribution is not only affected by ocean heat loss and gain, and biological production and respiration, but also by sea-ice formation and melting, river discharge, and shelf–basin interactions (cf. Bates and Mathis, 2009, and

55 references therein). However, CO_2 measurements are sparse in this very heterogeneous
56 area (Fig. 2), and hence the existing air–sea CO_2 flux estimates in the Arctic are poorly
57 constrained (Bates and Mathis, 2009; Schuster et al., 2013; Yasanuka et al., 2016).
58 As global warming progresses, melting of sea ice will increase the area of open water
59 and enhance the potential for atmospheric CO_2 uptake (e.g., Bates et al., 2006; Gao et
60 al., 2012). However, other processes could suppress CO_2 uptake. For example,
61 increasing seawater temperatures, declining buffer capacity due to the freshening of
62 Arctic surface water by increased river runoff and melting of sea-ice, and increased
63 vertical mixing supplying high-CO_2 water to the surface will all result in a tendency for
64 reduced uptake (Bates and Mathis, 2009; Cai et al., 2010; Chierici et al., 2011; Else et
65 al., 2013; Bates et al. 2014; Fransson et al., 2017). The combined effect of all these
66 processes on ocean CO_2 uptake has not yet been clarified for the Arctic.
67 Yasunaka et al. (2016) prepared monthly maps of air–sea CO_2 fluxes from 1997 to
68 2013 for the Arctic north of 60° N by applying, for the first time, a self-organizing map
69 (SOM) technique to map pCO_{2w} in the Arctic Ocean. The advantage of the SOM
70 technique is its ability to empirically determine relationships among variables without
71 making any a priori assumptions (about what types of regression functions are
72 applicable, and for which sub-regions the same regression function can be adopted, for

73 example). The SOM technique has been shown to reproduce the distribution of pCO_{2w}
74 from unevenly distributed observations better than multiple regression methods
75 (Lefèvre et al., 2005; Telszewski et al., 2009). The uncertainty of the CO_2 flux estimated
76 by Yasunaka et al. (2016), however, was large (±3.4–4.6 mmol m^{-2} d^{-1}), and the
77 estimated CO_2 uptake in the Arctic Ocean was smaller than the uncertainty (180 ± 210
78 TgC y^{-1}). One possible reason for the large uncertainties is that no direct proxies for the
79 effect of biological processes on pCO_{2w} were used in that study, leading to an
80 underestimation of the seasonal amplitude of pCO_{2w}.
81 Remotely sensed chlorophyll-a concentrations (Chl-a) has been used in several
82 pCO_{2w} mapping efforts as a direct proxy for the effect of primary production. For
83 example Chierici et al. (2009) produced pCO_{2w} algorithms for the subpolar North
84 Atlantic during the period from May to October and found that the inclusion of Chl-a
85 improved the fit substantially. Measurements in several areas of the Arctic show that
86 relationships between pCO_{2w} and Chl-a occur also in this region. They correlate
87 negatively (Gao et al., 2012; Ulfsbo et al., 2014), as expected from the drawdown of
88 CO_2 during photosynthesis, but exceptions do occur; in coastal regions the correlation is
89 positive (Mucci et al., 2010).
90 Several studies have demonstrated that Chl-a in the Arctic can be estimated from

satellite remote sensing reflectance (Rrs) (e.g. Arrigo and Dijken, 2004; Cota et al., 2004). Perrette et al. (2011) showed that satellite-derived Chl-a successfully captured a phytoplankton bloom in the ice-edge region. Changes in the seasonal cycle from a single peak to a double peak of Chl-a have also been detected and are likely a consequence of the recent sea-ice loss in the Arctic (Ardyna et al., 2014). However, the available products (e.g. NASA's OceanColor dataset) in the Arctic include large uncertainty and many missing values because of sea ice, low angle of sun-light and cloud cover, and are also prone to error due to the co-occurrence of large colored dissolved organic matter (CDOM) and total suspended matter (TSM) concentrations (e.g., Matuoka et al., 2007; Lewis et al., 2016). Here we deal with these issues by using several Chl-a algorithms optimised for the Arctic and others, and by excluding Chl-a data from grid cells potentially affected by CDOM and TSM. Calculated Chl-a values were then interpolated Chl-a so as to fit with the original data. Using these data, we examined the relationship between pCO_{2w} and Chl-a in the Arctic Ocean and its adjacent seas, and computed monthly air–sea CO_2 flux maps for regions north of 60° N using a SOM technique similar to that of Yasunaka et al. (2016), and with Chl-a added to the SOM process.

2. Data

2.1. $pCO_{2\,w}$ measurements

We used fugacity of CO_2 (fCO_{2w}) observations from the Surface Ocean CO_2 Atlas version 4 (SOCATv4; Bakker et al., 2016; http://www.socat.info/; 1,983,799 data points from >60° N), and pCO_{2w} observations from the Global Surface pCO_2 Database Version 2014 (LDEOv2014; Takahashi et al., 2015; http://cdiac.ornl.gov/oceans/LDEO_Underway_Database/; 302,150 data points from >60° N). In the LDEO database, pCO_{2w} is based on measured CO_2 mixing ratio in a parcel of air equilibrated with sea-water sample, and computed assuming CO_2 as an ideal gas, whereas in the SOCAT, fCO_2 is obtained considering the non-ideality from CO_2-CO_2 and CO_2-H_2O molecular interactions. Because of ambiguities in the CO_2-H_2O interaction corrections, the SOCAT fCO_{2w} values are converted to pCO_{2w} values (a correction of <1 %), and then combined them with the LDEO pCO_{2w} values. When data points were duplicated in the SOCAT and LDEO datasets, the SOCAT version was used, except for the data obtained from onboard the USCGC *Healy* as these have been reanalyzed by Takahashi et al. (2015). Altogether 200,409 duplicates were removed. We also used shipboard pCO_{2w} data obtained during cruises of the R/V *Mirai* of the Japan Agency for Marine-Earth Science and Technology (JAMSTEC) that have not yet been

127 included in SOCATv4 or LDEOv2014 (cruises MR09_03, MR10_05, MR12_E03, and
128 MR13_06; available at http://www.godac.jamstec.go.jp/darwin/e; 95,725 data points
129 from >60° N). In total, we used 2,181,265 pCO_{2w} data points, 33 % more than used by
130 Yasunaka et al. (2016).
131 To further improve the data coverage, especially for the ice-covered regions, we also
132 used 2166 pCO_{2w} values calculated from dissolved inorganic carbon (DIC) and total
133 alkalinity (TA) data extracted from the Global Ocean Data Analysis Project version 2
134 (GLODAPv2; Key et al., 2015; Olsen et al., 2016; http://www.glodap.info). 90% of
135 these data were obtained at cruises without underway pCO_{2w} data. We extracted values
136 of samples obtained from water depths shallower than 10 m, or the shallowest values
137 from the upper 30 m of each cast if there were no values from above 10 m. There are
138 1795 data points above 10 m depth, 296 in the 10–20 m range, and 75 in the 20–30 m
139 range. This resulted in 94 % more calculated pCO_{2w} values than used by Yasunaka et al.
140 (2016), and altogether the number of directly measured and calculated data points used
141 here is 33% more than used in Yasunaka et al. (2016). The CO2SYS program (Lewis
142 and Wallace, 1998; van Heuven et al., 2009) was used for the calculation with the
143 dissociation constants reported by Lueker et al. (2000) and Dickson (1990).
144 We checked the difference between calculated pCO_{2w} and measured pCO_{2w} using the

145 data from cruises with both bottle DIC/TA samples and underway pCO_{2w} available
146 (10% of the bottle samples, i.e., 245 pairs). Mean value for the calculated pCO_{2w} values
147 from bottle DIC/TA samples from the upper 30 m was 299 ± 42 μatm, and that for the
148 corresponding directly measured pCO_{2w} values from underway observation generally at
149 4–6m was 289 ± 11 μatm. The mean values are slightly higher for calculated pCO_{2w}
150 values than for measured ones, but the difference is smaller than the standard deviation
151 and the uncertainties of the calculation (the latter of which is 14 μatm; see Section 4.2).
152 The difference between calculated and measured pCO_{2w} is not dependent on the depth
153 where the TA/DIC samples were obtained. It was 10 ± 31 μatm for samples from above
154 10 m, 7 ± 27 μatm for samples from 10–20 m, and 11 ± 47 μatm for samples from 20–
155 30 m.

156 The availability of pCO_{2w} data (measured and calculated) varies spatially and
157 temporally (Fig. 2). Most of the available data are from the subpolar North Atlantic, the
158 Greenland Sea, the Norwegian Sea, the Barents Sea, and the Chukchi Sea while much
159 less data are available for the Kara Sea, the Laptev Sea, the East Siberian Sea, and the
160 Eurasian Basin. The number of pCO_{2w} data increased after 2005, but there are also a
161 substantial number of data from before 2004.

162

163 2.2. Other data

164 To calculate Chl-a, we used merged Rrs data from the SeaWiFS, MODIS-Aqua, MERIS,
165 and VIIRS ocean color sensors processed and distributed by the GlobColour Project
166 (Maritorena et al., 2010; http://hermes.acri.fr/index.php?class=archive). For
167 compatibility with the spatio-temporal resolution of the gridded pCO_{2w} data (see below
168 Sect. 3.3), we selected monthly mean Rrs data with a spatial resolution of 1° (latitude) ×
169 1° (longitude).

170 Sea surface temperature (SST) data were extracted from the National Oceanic and
171 Atmospheric Administration (NOAA) Optimum Interpolation SST Version 2 (Reynolds
172 et al., 2002; http://www.esrl.noaa.gov/psd/data/gridded/data.noaa.oisst.v2.html). These
173 data are provided at a resolution of 1° × 1° × 1 month. Sea surface salinity (SSS) data
174 were retrieved from the Polar Science Center Hydrographic Climatology version 3.0,
175 which also has a resolution of 1° × 1°× 1 month (Steele et al., 2001;
176 http://psc.apl.washington.edu/nonwp_projects/PHC/Climatology.html). Sea ice
177 concentration (SIC) data were obtained from the NOAA/National Snow and Ice Data
178 Center Climate Data Record of Passive Microwave Sea Ice Concentration version 2,
179 which has a resolution of 25 km × 25 km × 1 month (Meier et al., 2013;
180 http://nsidc.org/data/G02202). These data were averaged into 1° × 1° × 1 month

grid-cells. Zonal mean data for the atmospheric CO_2 mixing ratio (xCO_{2a}) were retrieved from the NOAA Greenhouse Gas Marine Boundary Layer Reference data product (Conway et al., 1994; http://www.esrl.noaa.gov/gmd/ccgg/mbl/index.html) and were interpolated into 1° × 1° × 1 month grid-cells. Both sea level pressure and 6-hourly 10-m wind speeds data were obtained from the U.S. National Centers for Environmental Prediction–Department of Energy Reanalysis 2 (NCEP 2) (Kanamitsu et al., 2002; http://www.esrl.noaa.gov/psd/data/gridded/data.ncep.reanalysis2.html). We also used the 6-hourly 10-m wind speeds from the U.S. National Centers for Atmospheric Prediction and the National Center for Atmospheric Research Reanalysis 1 (NCEP1) (Kalnay et al., 1996; https://www.esrl.noaa.gov/psd/data/gridded/data.ncep.reanalysis.html) when the gas transfer velocity was optimized for NCEP2 wind (see Section 3.5 below).

Surface nitrate measurements were extracted from GLODAPv2 (Key et al., 2015; Olsen et al., 2016) and the World Ocean Database 2013 (WOD; Boyer et al., 2013). When data points were duplicated in the GLODAPv2 and WOD datasets, the GLODAPv2 version was used as this has been subjected to more extensive quality control.

3. Methods

3.1. Calculation of chlorophyll-a concentrations

Chl-a was calculated from Rrs by using the Arctic algorithm developed by Cota et al. (2004). Several assessments have shown that this algorithm has a large uncertainty (e.g., Matsuoka et al., 2007; Lewis et al., 2016), and therefore the sensitivity of our results to this choice was evaluated by using two alternative algorithms for Chl-a: the standard algorithm of O'Reilly et al. (1998), and the coastal algorithm, of Tassan (1994).

To ensure that we were working with Rrs data relatively unaffected by CDOM and TSM, the Chl-a data were masked following the method of Siswanto et al. (2013). Briefly, the Rrs spectral slope between 412 and 555 nm ($Rrs_{555\text{-}412\ slope}$; $sr^{-1}\ nm^{-1}$) was plotted against logarithmically transformed Chl-a. Based on the scatter plot of log(Chl-a) and $Rrs_{555\text{-}412\ slope}$, we then defined a boundary line separating phytoplankton-dominated grid-cells ($Rrs_{555\text{-}412\ slope}$ < boundary value) from potentially non-phytoplankton-dominated grid-cells ($Rrs_{555\text{-}412\ slope} \geq$ boundary value) by:

$$Rrs_{555\text{-}412\ slope} = -0.000003\{\log(\text{Chl-a})\}^2 + 0.00002\{\log(\text{Chl-a})\} + 0.00006. \quad (1)$$

Grid-cells were considered invalid and masked out if 1) $Rrs_{555\text{-}412\ slope} \geq$ boundary value,

217 or 2) Rrs at 555nm (Rrs_{555}) > 0.01 sr^{-1} (or normalized water-leaving radiance > 2 mW
218 cm^{-2} μm^{-1} sr^{-1}; see Siswanto et al., 2011 and Moore et al., 2012). This criterion masked
219 2% of all Chl-a data.
220 The criteria described in the previous paragraph could mask out grid-cells having
221 coccolithophore blooms, which are sometimes observed in the Arctic Ocean (e.g.,
222 Smyth et al., 2004), as they also have Rrs_{555} > 0.01 sr^{-1} (Moore et al., 2012). Unlike
223 waters dominated by non-phytoplankton particles, whose Rrs spectral shape peaks at
224 555 nm, the Rrs spectral shape of waters with coccolithophore blooms peaks at 490 or
225 510 nm (see Iida et al., 2002; Moore et al., 2012). Therefore, grid-cells with Rrs spectral
226 peaks at 490 or 510 nm (already classified using the criteria of Rrs at 490nm (Rrs_{490}) >
227 Rrs at 443nm (Rrs_{443}) and Rrs at 510nm (Rrs_{510}) > Rrs_{555}) were considered as
228 coccolithophore grid-cells, and were reintroduced. 8% of the masked Chl-a data were
229 reintroduced by this criterion.
230
231 3.2. Chlorophyll-a interpolation
232 Chl-a values are often missing because of cloud cover, low angle of sunlight, or sea ice.
233 For the period and area analyzed here, data are missing for 86 % of the space and time
234 grid-cells. Because pCO_{2w} mapping requires a complete Chl-a field without missing

values, we interpolated the Chl-a data as follows; 1) Chl-a was set to 0.01 mg m^{-3} (minimum value of Chl-a) in high-latitude regions in winter when there was no light (north of 80° N in December and January, and north of 88° N in November and February). 2) Whenever SIC was greater than 99 %, Chl-a was set to 0.01 mg m^{-3} (full ice coverage, thus minimum Chl-a). We chose the strict criterion of SIC > 99 % because weak but significant primary production has been found to occur under the sea ice in regions with SIC around 90 % (Gosselin et al., 1997; Ulfsbo et al., 2014; Assmy et al., 2017). 3) The remaining grid-cells with missing data were filled, wherever possible, using the average of Chl-a in the surrounding grid-cells within ±1° latitude and ±1° longitude; this mainly compensated for missing Chl-a values due to cloud cover or grid-cells masked out as potentially affected by CDOM and TSM. 4) Parts of the remaining missing Chl-a values, mainly for the pre-satellite period of January–August 1997, were set to the monthly climatological Chl-a values based on the 18-year monthly mean from 1997 to 2014. 5) The final remaining missing Chl-a data, mainly for the marginal sea-ice zone, were generated by linear interpolation using surrounding data. With each interpolation step the number of the grid-cells with missing data decreased; 23 % of grid-cells without Chl-a data were filled by the first step, and the subsequent steps provided data for the remaining 12, 8, 5, and 52 %.

253

254 3.3. Gridding of pCO_2 data

255 In order to bring the individual pCO_{2w} data to the same resolution as the other input data,
256 they were gridded to 1° × 1° × 1 month grid-cells covering the years from 1997 to 2014.
257 This was carried out using the same three-step procedure of Yasunaka et al. (2016) as
258 this excludes values that deviate largely from the long-term mean in the area of each
259 grid cell. In short, first, anomalous values were screened in the following manner. We
260 calculated the long-term mean and its standard deviation for a window size of ±5° of
261 latitude, ±30° of longitude, and ±2 months (regardless of the year) for each 1° × 1° × 1
262 month grid-cell. We then eliminated the data in each grid-cell that differed by more than
263 three standard deviations from this long-term mean. In the second step, we recalculated
264 the long-term mean and its standard deviation using a smaller window size of ±2° of
265 latitude, ±10° of longitude, and ±1 month (regardless of the year) for each 1° × 1° × 1
266 month grid-cell, and eliminated data that differed from that long-term mean by more
267 than three standard deviations. In the final step the mean value of the remaining data in
268 each 1° × 1° × 1 month grid cell for each year from 1997 to 2014 was calculated. This
269 procedure identified in total about 0.5 % of the data as extreme values. These may well
270 be correct observations, but likely reflect small spatial scale and/or short time scale

271 variations that can are quite atypical of the large-scale variability of interest in this study.
272 These excluded values were randomly distributed in time and space.
273 Although some studies have used pCO_{2w} normalized to a certain year, based on the
274 assumption of a constant rate of increase for pCO_{2w} (e.g., Takahashi et al., 2009), we
275 used "non-normalized" pCO_{2w} values from all years; therefore, in our analysis pCO_{2w}
276 can increase both non-linearly in time and non-uniformly in space.
277
278 3.4. pCO_2 estimation using a self-organizing map
279 We estimated pCO_{2w} by the SOM technique used by Yasunaka et al. (2016), but with
280 Chl-a as an added training parameter to the SOM in addition to SST, SSS, SIC, xCO_{2a},
281 and geographical position X (=sin[latitude] × cos[longitude]) and Y (=sin[latitude] ×
282 sin[longitude]). Chl-a, SST, SSS, and SIC are closely associated with processes causing
283 variation in pCO_{2w}, such as primary production, warming/cooling, mixing, and
284 freshwater input, and represent spatio-temporal pCO_{2w} variability at seasonal to
285 interannual time-scales. Including the xCO_{2a} enables the SOM to reflect the pCO_{2w}
286 time-trend in response to the atmospheric CO_2 changes including large seasonal
287 variation and continued anthropogenic emissions. In several previous studies the
288 anthropogenic pCO_{2w} increase has been assumed to be steady and homogeneous, and

289 subtracted from the original pCO_{2w} data and added to the estimated pCO_{2w} (Nakaoka et
290 al. 2013; Zheng et al. 2014). However, the occurrence of steady and homogeneous
291 pCO_{2w} trends has not yet been demonstrated in the Arctic Ocean and using xCO_{2a} as a
292 training parameter in the SOM, similar to Landschutzer et al. (2013, 2014) is preferable.
293 Finally, the inclusion of geographical position among the training parameters can
294 prevent systematic spatial biases (Yasunaka et al., 2014). Compared to other efforts
295 mapping pCO_{2w} using the SOM technique such as those by Telszewski et al. (2009) and
296 Nakaoka et al. (2013), we used xCO_{2a}, and geographical position as training parameters
297 while we did not use mixed layer depth because of lack of reliable data in the Arctic.
298 Briefly, the SOM technique was implemented as follows: first, the approximately one
299 million 1° × 1° × 1 month grid-cells in the analysis region and period were assigned to
300 5000 groups, which are called “neurons”, of the SOM by using the training parameters.
301 Then, each neuron was labeled, whenever possible, with the pCO_{2w} value of the
302 grid-cell where the Chl-a, SST, SSS, SIC, xCO_{2a}, and X and Y values were most similar
303 to those of the neuron. Finally, each grid-cell in the analysis region and period was
304 assigned the pCO_{2w} value of the neuron whose Chl-a, SST, SSS, SIC, xCO_{2a}, and X and
305 Y values were most similar to those of that grid-cell. If the most similar neuron was not
306 labeled with a pCO_{2w} value, then the pCO_{2w} value of the neuron that was most similar

307 *and* labeled was used. That case often happened in periods and regions without any
308 observed data. A detailed description of the procedure can be found in Telszewski et al.
309 (2009) and Nakaoka et al. (2013).
310
311 3.5. Calculation of air–sea CO_2 fluxes
312 We calculated monthly air–sea CO_2 flux (F) values from the pCO_{2w} values estimated in
313 Sect. 3.4 by using the bulk formula:
314
315 $$F = kL(pCO_{2w} - pCO_{2a}) , \quad (2)$$
316
317 where k is the gas transfer velocity and L is the solubility of CO_2. The solubility of CO_2
318 (L) was calculated as a function of SST and SSS (Weiss, 1974). We converted the
319 interpolated NOAA marine boundary layer xCO_{2a} data (Sect. 2.2) to pCO_{2a} by using
320 monthly sea-level pressure data and the water-vapor saturation pressure calculated from
321 monthly SST and SSS (Murray, 1967).
322 The gas transfer velocity k was calculated by using the formula of Sweeney et al.
323 (2007):
324

$$k = 0.19\,(Sc/660)^{-0.5} \langle W_{NCEP2}^2 \rangle\,, \quad (3)$$

where Sc is the Schmidt number of CO_2 in seawater at a given SST, calculated according to Wanninkhof (2014), "< >" denotes the monthly mean, and $\langle W_{NCEP2}^2 \rangle$ is the monthly mean of the second moment of the NCEP2 6-hourly wind speed. The coefficient 0.19, which is the global average of $0.27\langle W_{NCEP1}^2 \rangle / \langle W_{NCEP2}^2 \rangle$, is based on the one determined by Sweeney et al. (2007) but optimized for NCEP2 winds, following the same method as Schuster et al. (2013) and Wanninkhof et al. (2013).

The suppression of gas exchange by sea ice was accounted for by correcting the air–sea CO_2 fluxes using the parameterization presented by Loose et al. (2009); the flux is proportional to $(1\text{-SIC})^{0.4}$. Following Bates et al. (2006), in the regions with SIC > 99 %, we used SIC = 99 % to allow for non-negligible rates of air–sea CO_2 exchange through leads, fractures, and brine channels (Semiletov et al., 2004; Fransson et al., 2017). This parameterization reduces the flux in fully ice covered waters (SIC > 99%) by 84%.

4. Uncertainty

4.1. Uncertainty in chlorophyll-a concentration data

Fig. 3 shows original and interpolated Chl-a for the year 2012 as an example. Overall,

343 the interpolated Chl-a data seems to fit well with the original data. Most interpolated
344 Chl-a data have low concentrations because of high SIC and lack of sunlight. The
345 average of the interpolated Chl-a values is 0.1 mg m^{-3}, and less than 5% of the
346 interpolated Chl-a values are >0.5 mg m^{-3} (cf. the average of the original Chl-a values is
347 1.1 mg m^{-3}, and 48% of the original Chl-a values are >0.5 mg m^{-3}). The previous
348 studies to estimate pCO_{2w} in high-latitudes assumed missing Chl-a as constant values
349 and ignored spatio-temporal variation of Chl-a (Landschutzer et al. 2013; Nakaoka et al.
350 2013). However, original Chl-a values in the ice-edge region are not small as captured
351 by Perrette et al. (2011), and those in the northernmost grids in winter, north of which
352 the original Chl-a values are missing, is far south of polar night region, since they are
353 missing not because of no sunlight but because of low-angles of sunlight (Fig. 3a).
354 Therefore, we believe interpolation is better than lowest constant values.
355 To validate our Chl-a interpolation, we repeated the interpolation after randomly
356 eliminating 10 % of the satellite Chl-a values. We then used the eliminated original
357 Chl-a data as independent data for the validation. Note that this comparison was done
358 where there were the original Chl-a data, i.e. the high Chl-a region. The root mean
359 square difference (RMSD) and correlation coefficient between the interpolated and the
360 independent original Chl-a data are 0.90 mg m^{-3} and 0.80, respectively. It means the

361 interpolated Chl-a, maybe not quantitatively, but qualitatively reproduced the original
362 Chl-a, and therefore is a meaningful parameter in the SOM process. Actually Chl-a data
363 improved the pCO_{2w} estimate, even though Chl-a values in many grid-cells were
364 interpolated values (see Sec. 5.4).
365 To evaluate our choice of Chl-a algorithm (i.e. the Arctic algorithm of Cota et al.,
366 2004), we compared its calculated Chl-a values with those determined by using the
367 standard algorithm of O'Reilly et al. (1998) and the coastal algorithm of Tassan (1994).
368 RMDS and correlation coefficient (r) between the original (i.e. non-interpolated) Chl-a
369 values are about 0.8 mg m^{-3} and 0.9, respectively (Table 1). For all the Chl-a values
370 including the interpolated data, they are about 0.4 mg m^{-3} and 0.9. The lower RMSD in
371 this case results from the fact that most of the interpolated Chl-a values have low
372 concentrations. This result means the Chl-a from the different algorisms, maybe not
373 quantitatively, but qualitatively consistent with each other. Since not absolute Chl-a
374 values but relative values affect the pCO_{2w} estimates in the SOM technique, the large
375 RMSD among the Chl-a does not result in the significant difference of the pCO_{2w}
376 estimates. Actually, the pCO_{2w} and CO_2 fluxes determined using Chl-a from any of
377 these algorithms as input to the SOM are consistent within their uncertainties (see Sects.
378 4.2 and 4.3 below). RMSDs between the observed and estimated pCO_{2w} are smallest in

379 pCO_{2w} estimate using Chl-a from the Arctic algorism, but the differences are quite small
380 (<1%).
381
382 4.2. Uncertainty of pCO_{2w} mapping
383 Fig. 4 compares observed and estimated pCO_{2w} (note that the spatial change visible in
384 Figs. 4a and 4b include differences generated by different seasonal coverage of data in
385 the various regions). Both observed and estimated pCO_{2w} tend to be higher in the
386 subpolar North Atlantic, the Laptev Sea, and the Canada Basin, and lower in the
387 Greenland Sea and the Barents Sea. However, the east–west contrast in the Bering Sea
388 and the contrast between the Canada Basin and the Chukchi Sea are weaker in our
389 estimates than in the observations, and mean bias and RMSD are relatively large in
390 those areas (Figs. 4c and 4d). The temporal changes in the observed and estimated
391 pCO_{2w} are in phase (Fig. 5a), although the variability of the estimated values is
392 somewhat suppressed compared to that of the observed data (Note that the temporal
393 change depicted in Fig. 5a also includes changes incurred by time variations in data
394 coverage). The mean bias and RMSD fluctuate seasonally but are at a constant level
395 over the years (Fig. 5b).
396 The correlation coefficient between estimated and observed pCO_{2w} is 0.82, and the

RMSD is 30 μatm, which is 9 % of the average and 58 % of the standard deviation of the observed pCO_{2w} values. This is a performance level categorized as "good" by Maréchal (2004). The differences between the estimated and observed values stem not only from the estimation error but also from the error of the gridded observed data. The uncertainty of the pCO_{2w} measurements is 2–5 μatm (Bakker et al., 2014), the uncertainty of the pCO_{2w} values calculated from dissolved inorganic carbon and total alkalinity, whose uncertainties are within 4 μmol kg^{-1} and 6 μmol kg^{-1}, respectively (Olsen et al., 2016), can be up to 14 μatm (Lueker et al., 2000), and the sampling error of the gridded pCO_{2w} observation data was determined from the standard errors of monthly observed pCO_{2w} in the 1° × 1° grid-cells, to 7 μatm (Yasunaka et al., 2016).

To validate our estimated pCO_{2w} values for periods and regions without any observed data, we repeated the mapping experiments after systematically excluding some of the observed pCO_{2w} data when labeling the neurons; four experiments were carried out, by excluding data (1) from 1997–2004, (2) from January to April, (3) from north of 80°N, and (4) from the Laptev Sea (90°E – 150°E), where there are only a few pCO_{2w} observations. We compared the pCO_{2w} estimates obtained in each experiment with the excluded observations and found that the pCO_{2w} estimates reproduced the general features of the excluded data, both spatially and temporally (not shown here). They

were also similar to the pCO_{2w} estimates obtained by using all observations, although the RMSDs between the estimates and the excluded observations are 54 μatm on average, which is 1.8 times the RMSDs of the estimates based on all observations. It means that our estimated pCO_{2w} reproduce the general features both in space and time even when and where there are no observed data, although the uncertainty in pCO_{2w} might be as large as 54 μatm in regions and periods without data. We used this uncertainty for pCO_{2w} estimates made by using the pCO_{2w} values of a less similar neuron.

4.3. Uncertainty of CO_2 flux estimates

Signorini and McClain (2009) estimated the uncertainty of the CO_2 flux resulting from uncertainties in the gas exchange parameterization to be 36 %, and that resulting from uncertainties in the wind data to be 11 %. The uncertainty for SIC is 5 % (Cavalieri et al., 1984; Gloersen et al., 1993; Peng et al., 2013). The standard error of the sea-ice effect on gas exchange was estimated to about 30 % by Loose et al. (2009). The uncertainty of pCO_{2a} is about 0.5 μatm (http://www.esrl.noaa.gov/gmd/ccgg/mbl/mbl.html), and that of pCO_{2w} was 30 μatm (Sect. 4.2); therefore, we estimated the uncertainty of ΔpCO_2 ($=pCO_{2w} - pCO_{2a}$) to be

34 % (average ΔpCO_2 in the analysis domain and period was −89 μatm). The overall uncertainty of the estimated CO_2 fluxes is thus 59 % ($[0.36^2 + 0.11^2 + 0.05^2 + 0.3^2 + 0.34^2]^{1/2}$) in sea-ice covered regions and 51 % ($[0.36^2 + 0.11^2 + 0.34^2]^{1/2}$) in ice-free regions. For estimates using the pCO_{2w} values of a less similar neuron, whose uncertainty in pCO_{2w} is 54 μatm and the uncertainty of the ΔpCO_2 estimates can be as high as 61 %, the uncertainty is 78 % ($[0.36^2 + 0.11^2 + 0.05^2 + 0.3^2 + 0.61^2]^{1/2}$) in sea-ice covered regions, and 72 % ($[0.36^2 + 0.11^2 + 0.61^2]^{1/2}$) in ice-free regions. The average of the estimated CO_2 flux in the analysis domain and period is 4.8 mmol m^{-2} d^{-1}; hence the uncertainty of the CO_2 flux estimate corresponds to 2.8 mmol m^{-2} d^{-1} in sea-ice covered regions and 2.4 mmol m^{-2} d^{-1} in ice-free regions. For estimates using the pCO_{2w} values of a less similar neuron, the uncertainty corresponds to 3.7 mmol m^{-2} d^{-1} in the sea-ice covered region and 3.5 mmol m^{-2} d^{-1} in ice-free regions.

5. Results and discussion

5.1. Relationship between pCO_2 and chlorophyll-a

Fig. 6 compares the observed pCO_{2w} and the original non-interpolated Chl-a in spring (March–May) and summer (July–September). In spring, when much of the Arctic Ocean is ice-covered, Chl-a is high in the Barents Sea and the Bering Strait (>1 mg m^{-3}). In

451 summer, when the ice cover is less extensive, Chl-a is high in the Chukchi Sea, the Kara
452 Sea, the Laptev Sea, and the East Siberian Sea (>1 mg m^{-3}) and especially high in the
453 coastal regions of the two latter (>2 mg m^{-3}). pCO_{2w} is high in the Norwegian Sea in
454 spring, and in the Kara Sea, the Laptev Sea and the Canada Basin during summer (>300
455 μatm). On the other hand, it is lower in the Chukchi Sea, Bering Strait area and the
456 sea-ice edge region of the Eurasian Basin in summer (<300 μatm). The overall
457 correlation between pCO_{2w} and Chl-a is negative where Chl-a ≤ 1 mg m^{-3} (70% of all
458 the data; correlation coefficient $r = -0.36$, $P < 0.01$), but there is no significant
459 relationship where Chl-a > 1 mg m^{-3} (Fig. 7). A similar situation was identified in the
460 subpolar North Atlantic by Olsen et al. (2008). It means that primary production
461 generally draws down the pCO_{2w}, but high Chl-a are not necessarily associated with the
462 low pCO_{2w} probably because high Chl-a usually appears in the coastal regions (Fig. 6b;
463 see below).

464 To determine the spatial variability of the relationship between pCO_{2w} and Chl-a, we
465 calculated the correlation coefficients between pCO_{2w} and Chl-a in a window of ±5° of
466 latitude, and ±30° of longitude for each monthly 1° × 1° grid-cell (Fig. 8a). The
467 correlations between pCO_{2w} and Chl-a are negative in the Greenland/Norwegian Seas
468 and over the Canada Basin. In the Greenland/Norwegian Seas, the correlation between

469 pCO_{2w} and Chl-a is strongly negative ($r < -0.4$) in spring and weakly negative ($-0.4 < r$
470 < 0) in summer. Chl-a there is higher in summer than in spring (Fig. 6b), whereas
471 nutrient concentrations are high in spring and low in summer (Fig. 8b). Taken together,
472 this suggest that primary production draws down the pCO_{2w} in spring, whereas in
473 summer the primary production mostly depends on regenerated nutrients (Harrison and
474 Cota, 1991) and the net CO_2 consumption is small, as also reported for the subpolar
475 North Atlantic (Olsen et al., 2008). Therefore the correlation between pCO_{2w} and Chl-a
476 becomes less negative. In the eastern Barents Sea, the Kara Sea and the East Siberian
477 Sea, and the Bering Strait, the correlations are positive because of water with high
478 pCO_{2w} and Chl-a in the coastal region subjected to river discharge (Murata, 2006;
479 Semiletov et al., 2007; Anderson et al., 2009; Manizza et al., 2011). In the Chukchi Sea,
480 the relationship is weak ($-0.2 < r < 0.2$), probably because the relationship is on smaller
481 spatial and temporal scales than those represented by the window size used here, as
482 shown by Mucci et al. (2010). The occurrence of calcifying plankton blooms in this
483 region, likely also weakens the correlation since the calcification increases pCO_{2w}
484 (Shutler et al., 2013; Fransson et al., 2017).

485 These results show that pCO_{2w} relates Chl-a, but the relationships are different
486 depending on the region and the season. It is difficult to represent such a complex

487 relationship using simple equations (e.g. multiple regression methods) because it needs
488 a priori assumptions of regression functions and of dividing the basin into sub-regions.
489 But the SOM technique can empirically induce the relationships without any of the a
490 priori assumptions, and therefore is suitable to represent such a complex relationship.
491
492 5.2. Spatiotemporal CO_2 flux variability
493 The 18-year annual mean CO_2 flux distribution shows that all areas of the Arctic
494 Ocean and its adjacent seas were net CO_2 sinks over the time period that we
495 investigated (Fig. 9). The annual CO_2 influx to the ocean was strong in the
496 Greenland/Norwegian Seas (9 ± 3 mmol m^{-2} d^{-1}; 18-year annual mean ± uncertainty
497 averaged over the area shown in Fig. 1), the Barents Sea (10 ± 3 mmol m^{-2} d^{-1}), and the
498 Chukchi Sea (5 ± 3 mmol m^{-2} d^{-1}). In contrast, influx was weak and not statistically
499 significantly different from zero in the Eurasian Basin, the Canada Basin, the Laptev
500 Sea and the East Siberian Sea. Our annual CO_2 flux estimates are consistent with those
501 reported by Yasunaka et al. (2016) and other previous studies (Bates and Mathis, 2009,
502 and references therein).
503 The estimated 18-year average CO_2 influx to the Arctic Ocean was 5 ± 3 mmol m^{-2} d^{-1}
504 , equivalent to an uptake of 180 ± 130 TgC y^{-1} for the ocean area north of 65° N,

505 excluding the Greenland/Norwegian Seas and Baffin Bay (10.7×10^6 km^2; see Fig. 1).
506 This accounts for 12% of the net global CO_2 uptake by the ocean of 1.5 Gt C yr^{-1}
507 (Gruber et al., 2009; Wanninkhof et al., 2013; Landschützer et al., 2014). It is within the
508 range of other estimates (81–199 TgC y^{-1}; Bates and Mathis, 2009), but close to the
509 upper bound. That is partly because the parameterization of the suppression effect by
510 sea ice used in this study. Using another parameterization which represents the SIC
511 effect linearly (Takahashi et al. 2009; Butterworth and Miller 2016), CO_2 uptake of the
512 Arctic Ocean was estimated to be 130 ± 110 TgC y^{-1}.
513 Fig. 10 shows the seasonal variation of the air-sea CO_2 fluxes and its controlling
514 factors (ΔpCO_2, wind speed and SIC; solubility is not shown as the impacts of its
515 variations are relatively small in this context) in the Greenland/Norwegian Seas, the
516 Barents Sea, the Chukchi Sea and the Arctic Ocean. In all of these regions the influxes
517 are strongest in October, when the winds strengthen with the approach of winter and the
518 pCO_{2w} and/or SIC are still as low as in the summer. In the Greenland/Norwegian Seas
519 and the Barents Sea the CO_2 influx shows a secondary maximum in February because
520 the strongest winds occur in that month, while in the Chukchi Sea and Arctic Ocean, the
521 winds are also strong but the flux is suppressed by the extensive sea-ice cover. All of
522 these regions are undersaturated with pCO_{2w} (i.e. negative ΔpCO_2) throughout all

seasons. The undersaturation is strongest in the Arctic Ocean, as this has the most extensive sea ice cover limiting the fluxes from the atmosphere and the strongest stratification, limiting the mixing of CO_2 rich subsurface waters into the surface ocean. The undersaturation typically shows a maximum (i.e. ΔpCO_2 is minimum) in late spring to early summer (May–June) when the spring bloom occur (Pabi et al. 2008), but not in the Arctic Ocean. Here the undersaturation reaches its minimum (ΔpCO_2 is the smallest) in late summer (August–September) at the time of minimum sea ice cover, since the seasonal decrease of pCO_2 in summer is larger in the air than in the sea. Overall, in the Greenland/Norwegian Seas and the Barents Sea the seasonal variations of the CO_2 flux is opposite to that expected from the seasonal ΔpCO_2 variations because it is the wind speed that governs most of the seasonal flux variations. In the Chukchi Sea, on the other hand, the CO_2 influx is strongest in summer, a consequence of the minimum sea-ice cover and strongest pCO_2 undersaturation. In the Arctic Ocean it is the SIC and wind speed that drive the seasonal flux variations. Seasonal variations of CO_2 flux are consistent with those of the previous studies (Yasunaka et al. 2016, and references therein), whereas those of pCO_{2w} become realistic (see Section 5.3 below).

Fig. 11 shows interannual variation of CO_2 flux and its driving factors in these four regions. The interannual variations of CO_2 flux and ΔpCO_2 are generally smaller than

541 the seasonal variations, and are often smaller than their respective uncertainty. In the
542 Greenland/Norwegian Sea, interannual variation of the CO_2 flux negatively correlates
543 with the wind speed (CO_2 influx to the ocean is large when the wind is strong; r = –
544 0.41), while interannual variation of ΔpCO_2 and sea ice change is small. In the Barents
545 Sea, the interannual variation of CO_2 flux correlates with ΔpCO_2 positively (r = 0.71)
546 and with SIC negatively (r = –0.50), while the correlation with wind speed is not
547 significant. Although low SIC enhance the air-sea CO_2 exchange due to increase of the
548 area of open water, it also associates with high SST and therefore high pCO_{2w} there. In
549 the Chukchi Sea, CO_2 influx to ocean is decreasing with the increasing of ΔpCO_2 (r =
550 0.87). High pCO_{2w} (>500 μatm) via storm-induced deep mixing events has been
551 sometimes observed in the Chukchi Sea after 2010 (Hauri et al. 2013; Taro Takahashi,
552 personal communication). Interannual variability of the CO_2 flux averaged over the
553 Arctic Ocean is small because the increasing ΔpCO_2 is compensated by the effect of sea
554 ice retreat (r = –0.70). Thus, the combined effect of sea-ice retreat and pCO_{2w} increase
555 on CO_2 flux varied among regions.

556 The CO_2 influx has been increasing in the Greenland Sea and northern Barents Sea,
557 and decreasing in the Chukchi Sea and southern Barents Sea (Fig. 12). The CO_2 flux
558 trend corresponds well with the ΔpCO_2 trend, which in turn corresponds well with the

559 SST trend. The increasing CO_2 influx in the northern Barents Sea also corresponds with
560 the sea-ice retreat. These results are similar to that for the previous estimates without
561 using Chl-a (see Fig. 10 in Yasunaka et al., 2016). It shows again that the combined
562 effect of sea-ice retreat and pCO_{2w} increase to the CO_2 flux is regionally different. In the
563 SOM process, the pCO_{2w} values observed in the latter period might be used for the
564 pCO_{2w} estimate in the former period where the pCO_{2w} measurements have not been
565 made, and therefore the trend in CO_2 influx might be affected by the spatio-temporal
566 distribution of the measurements. To confirm this is not the case, we checked that the
567 spatial distribution of the pCO_{2w} trend did not correspond to the year when the first
568 observation was conducted (see supplement).
569
570 5.3. Impact of incorporating chlorophyll-a data in the SOM
571 To determine the impact of including Chl-a data in the SOM process, the analyses were
572 repeated without Chl-a data. The RMSD of the resulting estimated pCO_{2w} values is 33
573 μatm, which is 3 μatm larger than the uncertainty of the estimates generated by
574 including Chl-a in the SOM. Chl-a data thus improved the pCO_{2w} estimate (namely, a
575 10 % reduction of RMSD), even though 40 % of the Chl-a data labeled with pCO_{2w}
576 observations were interpolated Chl-a values.

577 Figs. S1 and S2 present the difference in bias and RMSD for pCO_{2w} estimated with
578 and without Chl-a; Fig. S1 shows the time-evolution and Fig. S2 shows the spatial
579 distribution. Both approaches typically underestimate pCO_{2w} in winter and overestimate
580 the summertime values, but these systematic biases are reduced when Chl-a are
581 included in the SOM (Fig. S1). Biases and RMSDs are reduced in the Canada basin, the
582 western Bering Sea, and the boundary region between the Norwegian Sea and the
583 subpolar North Atlantic (Fig. S2). As a result the strong east–west contrast in the Bering
584 Sea and the contrast between the Canada Basin and the Chukchi Sea (see Fig. 4) are
585 better represented when Chl-a is included. Taken together, inclusion of Chl-a when
586 estimating pCO_{2w} yields not only better representation of the pCO_{2w} decline in spring
587 and summer but also improves the representation of the spatio-temporal pCO_{2w}
588 distribution. Technically, these improvements come from the fact that Chl-a as a training
589 parameter can separate high Chl-a region/time and low Chl-a region/time into different
590 neurons, which contaminated in the same neurons trained without Chl-a. For example,
591 since Chl-a is high in spring but SST and SIC are still in the similar levels with winter,
592 the grid-cells in spring and winter would be classified into the separate neurons when
593 Chl-a is included as a training parameter, but in the same neuron when Chl-a is not
594 included. As a result, without Chl-a, the estimated pCO_{2w} in spring tends to be similar to

595 the pCO_{2w} in winter, and the pCO_{2w} in winter tends to be similar to that in spring. And
596 therefore the contrast between winter and spring is weakened without Chl-a.
597 The seasonal cycles of pCO_{2w} estimates derived with the inclusion of Chl-a have a
598 larger amplitude than the uncertainties, whereas the uncertainties are larger than the
599 seasonal amplitude when pCO_{2w} is derived without Chl-a (upper panels of Fig. 13). The
600 difference is caused by the fact that the seasonal cycle of pCO_{2w} in each region
601 reproduces the observed cycle better when Chl-a was included (lower panels of Fig. 13).
602 Note that the much larger seasonal amplitude in the lower panels is an artefact generated
603 by the seasonal bias in sampling locations; in winter most measurements are obtained at
604 low latitudes where pCO_{2w} is typically higher than at high latitudes.
605 Compared to the CO_2 influx estimates by Yasunaka et al. (2016), the winter CO_2
606 influx in the Greenland/Norwegian Seas estimated including Chl-a is about 3 mmol m^{-2}
607 d^{-1} less than that calculated without using Chl-a (Fig. 14), but this difference is smaller
608 than the uncertainties. The CO_2 fluxes in the other area are quite similar with each
609 estimate, while their uncertainties are smaller in the present estimates.
610 The inclusion of Chl-a data also reduced the uncertainty of the estimated annual
611 air-sea CO_2 flux integrated over the entire Arctic Ocean. Compared to the flux estimate
612 determined by Yasunaka et al. (2016) of 180 ± 210 TgC y^{-1}, the CO_2 uptake in the

613 Arctic Ocean estimated here is significant within its uncertainty (180 ± 130 TgC y^{-1}).
614 This improvement is the result of 1) the inclusion of Chl-a data in the SOM process
615 (which reduced the uncertainty by 23 %); 2) the separate uncertainty estimates for
616 ice-free and ice-covered regions (8 %); and 3) the addition of new observational pCO_{2w}
617 data (7 %). Reducing the uncertainty of this quantification is a key contribution to the
618 larger work of constraining the global carbon budget (e.g., Le Quere et al., 2016).
619 Because the Arctic is an important CO_2 sink, quantifying its fluxes and minimizing the
620 uncertainty is of great scientific value.
621
622 5.4. Toward further reduction of the uncertainty
623 The addition of new observational data from SOCATv4 and GLODAPv2 reduced the
624 overall uncertainty in the mapped pCO_{2w}: a 33 % increase in the number of observations
625 induced a 7 % reduction in the uncertainty. However, there are still few observations in
626 the Kara Sea, the Laptev Sea, the East Siberian Sea and the Eurasian Basin (Fig. 2). To
627 improve our understanding of the variability in air–sea CO_2 fluxes in the Arctic, it is of
628 critical importance to obtain additional ocean CO_2 measurements to fill these data gaps,
629 and that these measurements are made publically available. Data synthesis activities like
630 SOCAT must be encouraged.

631 In the present study, we discussed the combined effect of sea-ice retreat and pCO_{2w}
632 change on the air-sea CO_2 flux. There are other factors that will induce the change of
633 CO_2 flux. For example, warmer temperature will lead to an increasing buffering
634 capacity while lower salinity will have the opposite effect and cause a decrease in
635 buffering capacity. In our current study, we used climatological-mean salinity for the
636 pCO_{2w} estimate because of lack of reliable year-to-year salinity data. That might be one
637 of the improvements for a future study.
638
639 **6. Conclusions**
640 By applying an SOM technique with the inclusion of Chl-a data to estimate pCO_{2w}, we
641 produced monthly maps of air–sea CO_2 fluxes from 1997 to 2014 for the Arctic Ocean
642 and its adjacent seas north of 60° N. Negative correlation between pCO_{2w} and Chl-a
643 meant that Chl-a is valuable parameter to represent primary production. Since the
644 relationship varied among seasons and regions, the SOM technique is better suited for
645 the mapping than a multiple linear regression approach. Adding Chl-a to the SOM
646 process improved representation of the seasonal cycle of pCO_{2w}, and therefore reduced
647 the uncertainty of the CO_2 flux estimates.
648 In the Greenland/Norwegian Seas and the Barents Sea the CO_2 influx was large in

649 autumn and winter because of the strong wind. In the Chukchi Sea, on the other hand,
650 the CO_2 influx was strong in summer and autumn, as a consequence of the low SIC and
651 strong pCO_{2w} undersaturation. Although interannual variation of the CO_2 influx was
652 smaller than the seasonal variation, the CO_2 influx has been increasing in the Greenland
653 Sea and northern Barents Sea, and decreasing in the Chukchi Sea and southern Barents
654 Sea.

655 A major goal of the carbon-cycle research community in recent years has been to
656 reduce the uncertainty in estimates of carbon reservoirs and fluxes. Our results
657 contribute to this in that CO_2 uptake in the Arctic Ocean is demonstrated with high
658 significance. The resulting estimate of the annual Arctic Ocean CO_2 uptake of 180 TgC
659 y^{-1} is significant with an uncertainty of ± 130 TgC y^{-1}. This is a substantial
660 improvement over earlier estimates, and is due mainly to the incorporation of Chl-a
661 data.

662 Assessment of the numerical models using our estimate of Arctic carbon uptake is
663 also an interesting topic since numerical models are poorly validated in the Arctic due to
664 the limited observations of biogeochemistry (Popova et al., 2012). However, such
665 experiments need thorough insight into the numerical models, which is beyond the
666 scope of this study. We hope to perform such comparisons in future studies.

667 The monthly CO_2 flux, pCO_{2w}, and interpolated Chl-a data presented in this paper
668 will be available at the JAMSTEC website
669 (http://www.jamstec.go.jp/res/ress/yasunaka/co2flux_v2).

670

671 **Acknowledgments**

672 We thank the many researchers and funding agencies responsible for the collection of
673 data and quality control for their contributions to SOCAT and GLODAPv2. We are
674 grateful for the use of the CO2SYS program obtained from the Ocean Carbon Data
675 System of NOAA National Centers for Environmental Information
676 (https://www.nodc.noaa.gov/ocads/oceans/CO2SYS/co2rprt.html), and SOM Toolbox
677 Version 2 developed by the Laboratory of Information and Computer Science at
678 Helsinki University of Technology (http://www.cis.hut.fi/projects/somtoolbox). We
679 thank ACRI-ST, France, for developing, validating, and distributing the GlobColour
680 data used in this work. This work was financially supported by the Arctic Challenge for
681 Sustainability (ArCS) Project funded by the Ministry of Education, Culture, Sports,
682 Science and Technology, Japan. Are Olsen was supported by grants from the Norwegian
683 Research Council (Subpolar North Atlantic Climate States [SNACS] 229752 and the
684 Norwegian component of the Integrated Carbon Observation System **[**ICOS-Norway]

245927). Mario Hoppema was partly supported by the German Federal Ministry of Education and Research (grant no. 01LK1224I; ICOS-D). Siv K. Lauvset acknowledges support from the Norwegian Research Council (VENTILATE, 229791) and the EU H2020 project AtlantOS (grant agreement no. 633211). Rik Wanninkhof and Taro Takahashi acknowledge support from the Office of Oceanic and Atmospheric Research (OAR) of the United States NOAA, including resources from the Ocean Observation and Monitoring Division of the Climate Program Office (fund reference100007298).

References

Anderson, L. G., Jutterström, S., Hjalmarsson, S., Wåhlström, I., and Semiletov, I. P.: Out-gassing of CO_2 from Siberian Shelf seas by terrestrial organic matter decomposition, Geophys. Res. Lett., 36, L20601, doi:10.1029/2009GL040046, 2009.

Ardyna, M., Babin, M., Gosselin, M., Devred, E., Rainville, L., and Tremblay, J.-É.: Recent Arctic Ocean sea ice loss triggers novel fall phytoplankton blooms, Geophys. Res. Lett., 41, 6207–6212, doi:10.1002/2014GL061047, 2014.

Arrigo, K. R., and van Dijken, G. L.: Annual cycles of sea ice and phytoplankton near Cape Bathurst, southeastern Beaufort Sea, Canadian Arctic, Geophys. Res. Lett., 31, L08304, doi:10.1029/2003GL018978, 2004.

703 Assmy P. M. Fernandez-Mendez, Duarte, P., Meyer, A., Randelhoff, A., Mundy, C. J.,
704 Olsen, L. M., Kauko, H. M., Bailey, A., Chierici, M., Cohen, L., Doulgeris, A. P.,
705 Ehn, J. K., Fransson, A., Gerland, S., Hop, H., Hudson, S. R., Hughes, N., Itkin, P. ,
706 Johnsen, G. , King, J. A., Koch, B. P. , Koenig, Z., Kwasniewski, S., Laney, S. R.,
707 Nicolaus, M., Pavlov, A. K., Polashenski, C. M., Provost, C., Rösel, A., Sandbu, M.,
708 Spreen, G., Smedsrud, L. H., Sundfjord, A., Taskjelle, T., Tatarek, A., Wiktor, J.,
709 Wagner, P. M., Wold, A., Steen, H., and Granskog, M. A.: Leads in Arctic pack ice
710 enable early phytoplankton blooms below snow-covered sea ice. Scientific Report,
711 7:40850, DOI: 10.1038/srep40850, 2017.

712 Bakker, D. C. E., Pfeil, B., Smith, K., Hankin, Olsen, A., Alin, C. Cosca, S. R.,
713 Harasawa, S., Kozyr, A., Nojiri, Y., O'Brien, K. M., Schuster, U., Telszewski, M.,
714 Tilbrook, B., Wada, C., Akl, J., Barbero, L., Bates, N., Boutin, J., Cai, W.-J., Castle,
715 R. D., Chavez, F. P., Chen, L., Chierici, M., Currie, K., de Baar, H. J. W., Evans, W.,
716 Feely, R. A., Fransson, A., Gao, Z., Hales, B., Hardman-Mountford, N., Hoppema,
717 M., Huang, W.-J., Hunt, C. W., Huss, B., Ichikawa, T., Johannessen, T., Jones, E. M.,
718 Jones, S., Jutterstrøm, S., Kitidis, V., Körtzinger, A., Lauvset, S. K., Lefèvre, N.,
719 Manke, A. B., Mathis, J. T., Merlivat, L., Metzl, N., Murata, A., Newberger, T., Ono,
720 T., Park, G.-H., Paterson, K., Pierrot, D., Ríos, A. F., Sabine, C. L., Saito, S.,

721 Salisbury, J., Sarma, V. V. S. S., Schlitzer, R., Sieger, R., Skjelvan, I., Steinhoff, T.,
722 Sullivan, K., Sun, H., Sutton, A. J., Suzuki, T., Sweeney, C., Takahashi, T., Tjiputra,
723 J., Tsurushima, N., van Heuven, S. M. A. C., Vandemark, D., Vlahos, P., Wallace, D.
724 W. R., Wanninkhof, R., and Watson, A. J.: An update to the Surface Ocean CO_2 atlas
725 (SOCAT version 2). Earth System Science Data, 6, 69–90,
726 doi:10.5194/essd-6-69-2014, 2014.
727 Bakker, D. C. E., Pfeil, B., Smith, K., Harasawa, S., Landa, C., Nakaoka, S., Nojiri, Y.,
728 Metzl, N., O'Brien, K. M., Olsen, A., Schuster, U., Tilbrook, B., Wanninkhof, R.,
729 Alin, S. R., Barbero, L., Bates, N. R., Bianchi, A. A., Bonou, F., Boutin, J., Bozec, Y.,
730 Burger, E., Cai, W.-J., Castle, R. D., Chen, L., Chierici, M., Cosca, C., Currie, K.,
731 Evans, W., Featherstone, C., Feely, R. A., Fransson, A., Greenwood, N., Gregor, L.,
732 Hankin, S., Hardman-Mountford, N. J., Harlay, J., Hauck, J., Hoppema, M., Humpt,
733 L., Monteiro, P., Munro, D., Murata, A., Newberger, T., Omar, A. M., Ono, T.,
734 Paterson, K., Pierrot, D., Robbins, L. L., Sabine, C. L., Saito, S., Salisbury, J.,
735 Schneider, B., Schlitzer, R., Sieger, R., Skjelvan, I., Steinhoff, T., Sullivan, K. F., St,
736 L., Monteiro, P., Munro, D., Murata, A., Newberger, T., Omar, A. M., Ono, T.,
737 Paterson, K., Pierrot, D., Robbins, L. L., Sabine, C. L., Saito, S., Salisbury, J.,
738 Schneider, B., Schlitzer, R., Sieger, R., Skjelvan, I., Steinhoff, T., Sullivan, K. F.,

739 Sutherland, S. C., Sutton, A. J., Sweeney, C., Tadokoro, K., Takahashi, T., Telszewski,
740 M., Van Heuven, S. M. A. C., Vandemark, D., Wada, C., Ward, B., and Watson, A. J.:
741 A multi-decade record of high quality fCO_2 data in version 3 of the Surface Ocean
742 CO_2 Atlas (SOCAT). Earth System Science Data, 8, 383–413.
743 doi:10.5194/essd-8-383-2016, 2016.
744 Bates, N. R., and Mathis, J. T.: The Arctic Ocean marine carbon cycle: evaluation of
745 air-sea CO_2 exchanges, ocean acidification impacts and potential feedbacks,
746 Biogeosciences, 6, 2433-2459, doi:10.5194/bg-6-2433-2009, 2009.
747 Bates, N. R., Moran, S. B., Hansell, D. A., and Mathis, J. T.: An increasing CO_2 sink in
748 the Arctic Ocean due to sea-ice loss, Geophys. Res. Lett., 33, L23609,
749 doi:10.1029/2006GL027028, 2006.
750 Bates, N. R., Garley, R., Frey, K. E., Shake, K. L., and Mathis J. T.: Sea-ice melt
751 CO_2-carbonate chemistry in the western Arctic Ocean: meltwater contributions to
752 air-sea CO_2 gas exchange, mixed layer properties and rates of net community
753 production under sea ice. Biogeosciences, 11, 6769–6789,
754 doi:10.5194/bg-11-6769-2014., 2014
755 Boyer, T. P., Antonov, J. I., Baranova, O. K., Coleman, C., Garcia, H. E., Grodsky, A.,
756 Johnson, D. R., Locarnini, R. A., Mishonov, A. V., O'Brien, T. D., Paver, C. R.,

757 Reagan, J. R., Seidov, D., Smolyar, I. V., and Zweng, M. M.: World Ocean Database
758 2013. Sydney Levitus, Ed.; Alexey Mishonov, Technical Ed.; NOAA Atlas NESDIS
759 72, 209 pp, 2013.
760 Butterworth, B. J., and Miller, S. D.: Air-sea exchange of carbon dioxide in the Southern
761 Ocean and Antarctic marginal ice zone. Geophys. Res. Lett., 43, 7223–7230,
762 doi:10.1002/2016GL069581, 2016.
763 Cai, W.J., Chen, L. Q., Chen, B. S., Gao, Z. Y., Lee, S. H., Chen, J. F., Pierrot, D.,
764 Sullivan, K., Wang, Y.C., Hu, X. P., Huang, W. J., Zhang, Y. H., Xu, S. Q., Murata, A.,
765 Grebmeier, J. M., Jones, E. P., and Zhang, H. S.: Decrease in the CO_2 uptake capacity
766 in an ice-free Arctic Ocean Basin. Science, 329, 556–559,
767 doi:10.1126/science.1189338, 2010.
768 Cavalieri, D. J., Gloersen, P., and Campbell, W. J.: Determination of sea ice parameters
769 with the NIMBUS-7 SMMR, J. Geophys. Res., 89, 5355–5369, 1984.
770 Chierici, M., Olsen, A., Johannessen, T., Trinañes, J., Wanninkhof, R.: Algorithms to
771 estimate CO_2 in the northern North Atlantic using observations, satellite and ocean
772 analysis data, Deep-Sea Res. II, 56, 630–639, doi:10.1016/j.dsr2.2008.12.01, 2009.
773 Chierici, M, Fransson, A., Lansard, B., Miller, L. A., Mucci, A., Shadwick, E., Thomas,
774 H., Tremblay, J.-E., and Papakyriakou, T.: The impact of biogeochemical processes

775 and environmental factors on the calcium carbonate saturation state in the
776 Circumpolar Flaw Lead in the Amundsen Gulf, Arctic Ocean. J. Geophys. Res., 116,
777 C00G09, doi:10.1029/2011JC007184, 2011.
778 Conway, T.J., Tans, P. P., Waterman, L. S., Thoning, K. W., Kitzis, D. R., Masarie, K. A.,
779 and Zhang, N.: Evidence for interannual variability of the carbon cycle from the
780 NOAA/CMDL global air sampling network. J. Geophys. Res., 99, 22831–22855,
781 1994.
782 Cota, G. F., Wang, J., and Comiso, J. C.: Transformation of global satellite chlorophyll
783 retrievals with a regionally tuned algorithm, Remote Sens. Environ. 89, 326–350,
784 doi:10.1016/j.rse.2004.01.005, 2004.
785 Dickson, A. G.: Standard potential of the reaction: AgCl(s) + 1/2H_2(g) = Ag(s) +
786 HCl(aq), and the standard acidity constant of the ion HSO_4^- in synthetic seawater
787 from 273.15 to 318.15 K. J. Chemical Thermodynamics, 22, 113–127, 1990.
788 Else, B. G. T., Galley, R. J., Lansard, B., Barber, D. G., Brown, K., Miller, L. A., Mucci,
789 A., Papakyriakou, T. N., Tremblay, J.-É., and Rysgaard, S.: Further observations of a
790 decreasing atmospheric CO_2 uptake capacity in the Canada Basin (Arctic Ocean) due
791 to sea ice loss, Geophys. Res. Lett., 40, 1132–1137, doi:10.1002/grl.50268, 2013.
792 Fransson, A., Chierici, M., Skjelvan, I., Olsen, A., Assmy, P., Peterson, A. K., Spreen, G.,

and Ward, B.: Effects of sea-ice and biogeochemical processes and storms on under-ice water fCO_2 during the winter-spring transition in the high Arctic Ocean: Implications for sea-air CO_2 fluxes. J. Geophys. Res., doi:10.1002/2016JC012478, 2017.

Gao, Z., Chen, L., Sun, H., Chen, B., and Cai, W.-J.: Distributions and air–sea fluxes of carbon dioxide in the Western Arctic Ocean, Deep-Sea Res. II, 81–84, 46–52, doi:10.1016/j.dsr2.2012.08.021, 2012.

Gloersen, P., Campbell, W. J., Cavalieri, D. J., Comiso, J. C., Parkinson, C. L., and Zwally, H. J.: Arctic and Antarctic sea ice, 1978–1987: Satellite passive-microwave observations and analysis, NASA Spec. Publ., 511, 290 pp, 1993.

Gosselin, M., Levasseur, M., Wheeler, P. A., Horner, R. A., and B. C. Booth: New measurements of phytoplankton and ice algal production in the Arctic Ocean, Deep-Sea Res. II, 44, 1623–1644, doi:10.1016/S0967-0645(97)00054-4, 1997.

Harrison, W. G., and Cota., G. F.: Primary production in polar waters: relation to nutrient availability, Polar Research, 10, 87–104, doi:10.1111/j.1751-8369.1991.tb00637.x, 1991.

Hauri, C., Winsor, P., Juranek, L. W., McDonell, A. M. P., Takahashi, T. and Mathis, J. T.: Wind-driven mixing causes a reduction in the strength of the continental shelf

811 carbon pump in the Chukchi Sea, Geophys. Res. Letters, 40, 5932-5936,
812 doi:10.1002/2013GL058267, 2013.
813 Iida, T., Saitoh, S. I., Miyamura, T., Toratani, M., Fukushima, H., and Shiga, N.:
814 Temporal and spatial variability of coccolithophore blooms in the eastern Bering Sea,
815 1998-2001, Prog. Oceanogr., 55, 165–175, 2002.
816 Kalnay, E., Kanamitsu, M., Kistler, R., Collins, W., Deaven, D., Gandin, L., Iredell, M.,
817 Saha, S., White, G., Woollen, J., Zhu, Y., Chelliah, M., Ebisuzaki, W., Higgins, W.,
818 Janowiak, J., Mo, K. C., Ropelewski, C., Wang, J., Leetmaa, A., Reynolds, R., Jenne,
819 R., and Joseph, D., The NCEP/NCAR 40-Year Reanalysis Project". Bull. Amer.
820 Meteor. Soc., 77, 437–471, 1996.
821 Kanamitsu, M., Ebisuzaki, W., Woollen, J., Yang, S-K, Hnilo, J. J., Fiorino, M., and
822 Potter, G. L., NCEP-DOE AMIP-II Reanalysis (R-2), Bull. Amer. Meteor. Soc., 83,
823 1631–1643, 2002.
824 Key, R.M., Olsen, A., van Heuven, S., Lauvset, S. K., Velo, A., Lin, X., Schirnick, C.,
825 Kozyr, A., Tanhua, T., Hoppema, M., Jutterström, S., Steinfeldt, R., Jeansson, E.,
826 Ishii, M., Perez, F. F., and T. Suzuki: Global Ocean Data Analysis Project, Version 2
827 (GLODAPv2), ORNL/CDIAC-162, ND-P093. Carbon Dioxide Information Analysis
828 Center, Oak Ridge National Laboratory, US Department of Energy, Oak Ridge,

829 Tennessee. doi: 10.3334/CDIAC/OTG.NDP093_GLODAPv2, 2015.
830 Le Quéré, C., Andrew, R. M., Canadell, J. G., Sitch, S., Korsbakken, J. I., Peters, G. P.,
831 Manning, A. C., Boden, T. A., Tans, P. P., Houghton, R. A., Keeling, R. F., Alin, S.,
832 Andrews, O. D., Anthoni, P., Barbero, L., Bopp, L., Chevallier, F., Chini, L. P., Ciais,
833 P., Currie, K., Delire, C., Doney, S. C., Friedlingstein, P., Gkritzalis, T., Harris, I.,
834 Hauck, J., Haverd, V., Hoppema, M., Klein Goldewijk, K., Jain, A. K., Kato, E.,
835 Körtzinger, A., Landschützer, P., Lefèvre, N., Lenton, A., Lienert, S., Lombardozzi,
836 D., Melton, J. R., Metzl, N., Millero, F., Monteiro, P. M. S., Munro, D. R., Nabel, J.
837 E. M. S., Nakaoka, S.-I., O'Brien, K., Olsen, A., Omar, A. M., Ono, T., Pierrot, D.,
838 Poulter, B., Rödenbeck, C., Salisbury, J., Schuster, U., Schwinger, J., Séférian, R.,
839 Skjelvan, I., Stocker, B. D., Sutton, A. J., Takahashi, T., Tian, H., Tilbrook, B., van
840 der Laan-Luijkx, I. T., van der Werf, G. R., Viovy, N., Walker, A. P., Wiltshire, A. J.,
841 and Zaehle, S.: Global Carbon Budget 2016, Earth Syst. Sci. Data, 8, 605-649,
842 https://doi.org/10.5194/essd-8-605-2016, 2016.
843 Landschützer, P., Gruber, N., Bakker, D. C. E., Schuster, U., Nakaoka, S., Payne, M. R.,
844 Sasse, T., and Zeng J., A neural network-based estimate of the seasonal to
845 inter-annual variability of the Atlantic Ocean carbon sink, Biogeosciences, 10, 7793–
846 7815, doi:10.5194/bg-10-7793-2013, 2013.

847 Landschützer, P., Gruber, N., Bakker, D. C. E., and Schuster, U.: Recent variability of
848 the global ocean carbon sink, Global Biogeochemical Cycles, 28, 927-949,
849 doi:10.1002/2014GB004853, 2014.
850 Lefèvre, N., Watson, A. J., and Watson, A. R.: A comparison of multiple regression and
851 neural network techniques for mapping in situ pCO_2 data, Tellus B, 57: 375–384.
852 doi:10.1111/j.1600-0889.2005.00164.x, 2005.
853 Lewis, E., and Wallace, D. W. R.: Program Developed for CO_2 System Calculations.
854 ORNL/CDIAC-105. Carbon Dioxide Information Analysis Center, Oak Ridge
855 National Laboratory, U.S. Department of Energy, Oak Ridge, Tennessee, 1998.
856 Lewis, K.M., Mitchell, B.G., van Dijken, G.L., and Arrigo, K.R.: Regional chlorophyll
857 a algorithms in the Arctic Ocean and their effect on satellite-derived primary
858 production estimates, Deep-Sea Res. II, 130, 17–24, doi:10.1016/j.dsr2.2016.04.020,
859 2016.
860 Loose, B., McGillis, W. R., Schlosser, P., Perovich, D., and Takahashi, T.: Effects of
861 freezing, growth, and ice cover on gas transport processes in laboratory seawater
862 experiments, Geophys. Res. Lett., 36, L05603, doi:10.1029/2008GL036318, 2009.
863 Lueker, T. J., Dickson, A. G., and Keeling, C. D.: Ocean pCO_2 calculated from
864 dissolved inorganic carbon, alkalinity, and equations for K1 and K2: validation based

865 on laboratory measurements of CO_2 in gas and seawater at equilibrium, Mar. Chem.,
866 70, 105–119, 2000.
867 Manizza, M., Follows, M. J., Dutkiewicz, S., Menemenlis, D., McClelland, J. W., Hill,
868 C. N., Peterson, B. J., and R. M. Key: A model of the Arctic Ocean carbon cycle, J.
869 Geophys. Res., 116, C12020, doi:10.1029/2011JC006998, 2011.
870 Maréchal, D., A soil-based approach to rainfall-runoff modelling in ungauged
871 catchments for England and Wales. PhD thesis, Cranfield University, U.K., 157 pp,
872 2004.
873 Maritorena, S., d'Andon, O. H. F., Mangin, A., and Siegel, D. A.: Merged satellite ocean
874 color data products using a bio-optical model: Characteristics, benefits and issues,
875 Remote Sensing of Environment, 114, 1791-1804, doi:10.1016/j.rse.2010.04.002,
876 2010.
877 Matsuoka, A., Huot, Y., Shimada, K., Saitoh, S., and Babin, M.: Bio-optical
878 characteristics of the western Arctic Ocean: Implications for ocean color algorithms,
879 Canadian J. Remote Sens., 33, 503–518, doi:10.5589/m07-059, 2007.
880 Meier, W., Fetterer, F., Savoie, M., Mallory, S., Duerr, R., and Stroeve, J.:
881 NOAA/NSIDC Climate Data Record of Passive Microwave Sea Ice Concentration.
882 Version 2, Boulder, Colorado USA: National Snow and Ice Data Center,

883 http://dx.doi.org/10.7265/N55M63M1, 2013.
884 Moore, T. S., Dowell, M. D., and Franz, B. A.: Detection of coccolithophore blooms in
885 ocean color satellite imagery: A generalized approach for use with multiple sensors,
886 Rem. Sens. Env., 117, 249–263, doi: 10.1016/j.rse.2011.10.001, 2012.
887 Mucci, A., Lansard, B., Miller, L. A., and Papakyriakou, T. N.: CO_2 fluxes across the
888 air-sea interface in the southeastern Beaufort Sea: Ice-free period, J. Geophys. Res.,
889 115, C04003, doi:10.1029/2009JC005330, 2010.
890 Murata, A.: Increased surface seawater pCO_2 in the eastern Bering Sea shelf: An effect
891 of blooms of coccolithophorid *Emiliania huxleyi*? Global Biogeochem. Cycles, 20,
892 GB4006, doi:10.1029/2005GB002615, 2006.
893 Murray, F. W.: On the computation of saturation vapor pressure. J. Applied Meteorology,
894 6, 203–204, 1967.
895 Nakaoka, S., Telszewski, M., Nojiri, Y., Yasunaka, S., Miyazaki, C., Mukai, H., and
896 Usui, N.: Estimating temporal and spatial variation of sea surface pCO_2 in the North
897 Pacific using a self organizing map neural network technique, Biogeosciences, 10,
898 6093-6106, doi:10.5194/bg-10-6093-2013, 2013.
899 Olsen, A., Brown, K. R., Chierici, M., Johannessen, T., and Neill, C.: Sea-surface CO_2
900 fugacity in the subpolar North Atlantic, Biogeosciences, 5, 535–547,

901 doi:10.5194/bg-5-535-2008, 2008.
902 Olsen, A., Key, R. M., van Heuven, S., Lauvset, S. K., Velo, A., Lin, X., Schirnick, C.,
903 Kozyr, A., Tanhua, T., Hoppema, M., Jutterström, S., Steinfeldt, R., Jeansson, E.,
904 Ishii, M., Pérez, F. F., and Suzuki, T.: The Global Ocean Data Analysis Project
905 version 2 (GLODAPv2) – an internally consistent data product for the world ocean,
906 Earth Syst. Sci. Data, 8, 297–323, 2016, doi:10.5194/essd-8-297-2016, 2016.
907 O'Reilly, J. E., Maritorena, S., Mitchell, B. G., Siegel, D. A., Carder, K. L., Garver, S. A.,
908 Kahru, M., and McClain, C.: Ocean color chlorophyll algorithms for SeaWiFS, J.
909 Geophys. Res., 103, 24937–24953, doi:10.1029/98JC02160, 1998.
910 Peng, G., Meier, W., Scott, D., and Savoie, M.: A long-term and reproducible passive
911 microwave sea ice concentration data record for climate studies and monitoring.
912 Earth Syst. Sci. Data 5: 311–318, http://dx.doi.org/10.5194/essd-5-311-2013, 2013.
913 Perrette, M., Yool, A., Quartly, G. D., and Popova, E. E.: Near-ubiquity of ice-edge
914 blooms in the Arctic, Biogeosciences, 8, 515–524, doi:10.5194/bg-8-515-2011, 2011.
915 Popova, E. E., Yool, A., Coward, A. C., Dupont, F., Deal, C., Elliott, S., Hunke, E., Jin,
916 M., Steele, M., and Zhang, J., What controls primary production in the Arctic Ocean?
917 Results from an intercomparison of five general circulation models with
918 biogeochemistry, J. Geophys. Res., 117, C00D12, doi:10.1029/2011JC007112, 2012.

919 Reynolds, R. W., Rayner, N. A., Smith, T. M., Stokes, D. C., and Wang, W.: An
920 improved in situ and satellite SST analysis for climate, J. Climate, 15, 1609–1625,
921 2002.
922 Schuster, U., McKinley, G. A., Bates, N., Chevallier, F., Doney, S. C., Fay, A. R.,
923 González-Dávila, M., Gruber, N., Jones, S., Krijnen, J., Landschützer, P., Lefèvre, N.,
924 Manizza, M., Mathis, J., Metzl, N., Olsen, A., Rios, A. F., Rödenbeck, C.,
925 Santana-Casiano, J. M., Takahashi, T., Wanninkhof, R., and Watson, A. J.: An
926 assessment of the Atlantic and Arctic sea–air CO_2 fluxes, 1990–2009,
927 Biogeosciences, 10, 607–627, doi:10.5194/bg-10-607-2013, 2013.
928 Shutler, J. D., Land, P. E., Brown, C. W., Findlay, H. S., Donlon, C. J., Medland, M.,
929 Snooke, R., and Blackford, J. C.: Coccolithophore surface distributions in the North
930 Atlantic and their modulation of the air-sea flux of CO_2 from 10 years of satellite
931 Earth observation data, Biogeosciences, 10, 2699–2709,
932 doi:10.5194/bg-10-2699-2013, 2013
933 Semiletov, I., Makshtas, A., Akasofu, S.-I., and Andreas, E. L: Atmospheric CO_2
934 balance: The role of Arctic sea ice, Geophys. Res. Lett., 31, L05121,
935 doi:10.1029/2003GL017996, 2004.
936 Semiletov, I. P., Pipko, I. I., Repina, I., and Shakhova, N. E.: Carbonate chemistry

937 dynamics and carbon dioxide fluxes across the atmosphere–ice–water interfaces in
938 the Arctic Ocean: Pacific sector of the Arctic, J. Mar. Syst., 66, 204–226,
939 doi:10.1016/j.jmarsys.2006.05.012, 2007.
940 Signorini, S. R., and McClain, C. R.: Effect of uncertainties in climatologic wind, ocean
941 pCO_2, and gas transfer algorithms on the estimate of global sea-air CO_2 flux, Global
942 Biogeochem. Cycles, 23, GB2025, doi:10.1029/2008GB003246, 2009.
943 Siswanto, E., Tang, J., Ahn, Y.-H., Ishizaka, J., Yoo, S., Kim, S.-W., Kiyomoto, Y.,
944 Yamada, K., Chiang, C., and Kawamura, H.: Empirical ocean color algorithms to
945 retrieve chlorophyll-a, total suspended matter, and colored dissolved organic matter
946 absorption coefficient in the Yellow and East China Seas, J. Oceanogr.,
947 doi:10.1007/s10872-011-0062-z, 2011.
948 Siswanto, E., Ishizaka, J., Tripathy, S. C., and Miyamura, K.: Detection of harmful algal
949 blooms of *Karenia mikimotoi* using MODIS measurements: a case study of
950 Seto-Inland Sea, Japan, Remote Sensing of Environment, 129, 185–196,
951 doi:10.1016/j.rse.2012.11.003, 2013.
952 Smyth, T. J., Tyrrell, T., Tarrant, B.: Time series of coccolithophore activity in the
953 Barents Sea, from twenty years of satellite imagery, Geophys. Res. Lett., 31, L11302,
954 doi:10.1029/2004GL019735, 2004.

955 Steele, M., Morley, R., and Ermold, W.: PHC: A global ocean hydrography with a high
956 quality Arctic Ocean, J. Climate, 14, 2079–2087, 2001.
957 Sweeney, C., Gloor, E., Jacobson, A. R., Key, R. M., McKinley, G., Sarmiento, J. L.,
958 and Wanninkhof, R.: Constraining global air-sea gas exchange for CO_2 with recent
959 bomb ^{14}C measurements, Global Biogeochem. Cycles, 21, GB2015,
960 doi:10.1029/2006GB002784, 2007.
961 Takahashi, T., Sutherland, S. C., Wanninkhof, R., Sweeney, C., Feely, R. A., Chipman,
962 D. W., Hales, B., Friederich, G., Chavez, F., Sabine, C., Watson, A., Bakker, D. C. E.,
963 Schuster, U., Metzl, N., Yoshikawa-Inoue, H., Ishii, M., Midorikawa, T., Nojiri, Y.,
964 Körtzinger, A., Steinhoff, T., Hoppema, M., Olafsson, J., Arnarson, T. S., Tilbrook,
965 B., Johannessen, T., Olsen, A., Bellerby, R., Wong, C. S., Delille, B., Bates, N. R., de
966 Baar, H. J. W.: Climatological mean and decadal changes in surface ocean pCO_2, and
967 net sea-air CO_2 flux over the global oceans. Deep-Sea Res. II, 56, 554–577, 2009.
968 Takahashi, T., Sutherland, S.C., and Kozyr, A.: Global Ocean Surface Water Partial
969 Pressure of CO_2 Database: Measurements Performed During 1957–2014 (Version
970 2014). ORNL/CDIAC-160, NDP-088(V2014). Carbon Dioxide Information Analysis
971 Center, Oak Ridge National Laboratory, U.S. Department of Energy, Oak Ridge,
972 Tennessee, doi: 10.3334/CDIAC/OTG.NDP088(V2014), 2015.

973 Tassan, S.: Local algorithms using SeaWiFS data for the retrieval of phytoplankton,
974 pigments, suspended sediment, and yellow substance in coastal waters, Applied Opt.,
975 33, 2369–2378, doi:10.1364/AO.33.002369, 1994.
976 Telszewski, M., Chazottes, A., Schuster, U., Watson, A. J., Moulin, C., Bakker, D.C.E.,
977 González-Dávila, M., Johannessen, T., Körtzinger, A., Lüger, H., Olsen, A., Omar, A.,
978 Padin, X. A., Ríos, A. F., Steinhoff, T., Santana-Casiano, M., Wallace, D. W. R., and
979 Wanninkhof, R.: Estimating the monthly pCO_2 distribution in the North Atlantic
980 using a self-organizing neural network, Biogeosciences, 6, 1405–1421,
981 doi:10.5194/bg-6-1405-2009, 2009.
982 Ulfsbo, A., Cassar, N., Korhonen, M., van Heuven, S., Hoppema, M., Kattner, G., and G.
983 Anderson, L.: Late summer net community production in the central Arctic Ocean
984 using multiple approaches, Global Biogeochem. Cycles, 28, 1129–1148,
985 doi:10.1002/2014GB004833, 2014.
986 van Heuven, S., Pierrot, D., Lewis, E., and Wallace, D. W. R.: MATLAB Program
987 Developed for CO2 System Calculations, ORNL/CDIAC-105b. Carbon Dioxide
988 Information Analysis Center, Oak Ridge National Laboratory, US Department of
989 Energy, Oak Ridge, Tennessee, 2009.
990 Wanninkhof, R.: Relationship between wind speed and gas exchange over the ocean, J.

991 Geophys. Res., 97(C5), 7373–7382, doi:10.1029/92JC00188, 1992.
992 Wanninkhof, R., Park, G. -H., Takahashi, T., Sweeney, C., Feely, R., Nojiri, Y., Gruber,
993 N., Doney, S. C., McKinley, G. A., Lenton, A., Le Quéré, C., Heinze, C., Schwinger,
994 J., Graven, H., and Khatiwala, S.: Global ocean carbon uptake: magnitude, variability
995 and trends, Biogeosciences, 10, 1983–2000, doi:10.5194/bg-10-1983-2013, 2013.
996 Wanninkhof, R.: Relationship between wind speed and gas exchange over the ocean
997 revisited, Limnol. Oceanogr.: Methods, 12, 351-362, 2014.
998 Weiss, R. F.: Carbon dioxide in water and seawater: the solubility of a non-ideal gas,
999 Mar. Chem., 2, 203–215, 1974.
1000 Yasunaka, S., Nojiri, Y., Nakaoka, S., Ono, T., Whitney, F. A., and Telszewski, M.:
1001 Mapping of sea surface nutrients in the North Pacific: Basin-wide distribution and
1002 seasonal to interannual variability, J. Geophys. Res. Oceans, 119, 7756–7771,
1003 doi:10.1002/2014JC010318, 2014.
1004 Yasunaka, S., Murata, A., Watanabe, E., Chierici, M., Fransson, A., van Heuven, S.,
1005 Hoppema, M., Ishii, M., Johannessen, T., Kosugi, N., Lauvset, S. K., Mathis, J. T.,
1006 Nishino, S., Omar, A. M., Olsen, A., Sasano, D., Takahashi, T., and Wanninkhof, R.:
1007 Mapping of the air–sea CO_2 flux in the Arctic Ocean and its adjacent seas:
1008 basin-wide distribution and seasonal to interannual variability, Polar Science, 10,

1009 323–334, doi:10.1016/j.polar.2016.03.006, 2016.

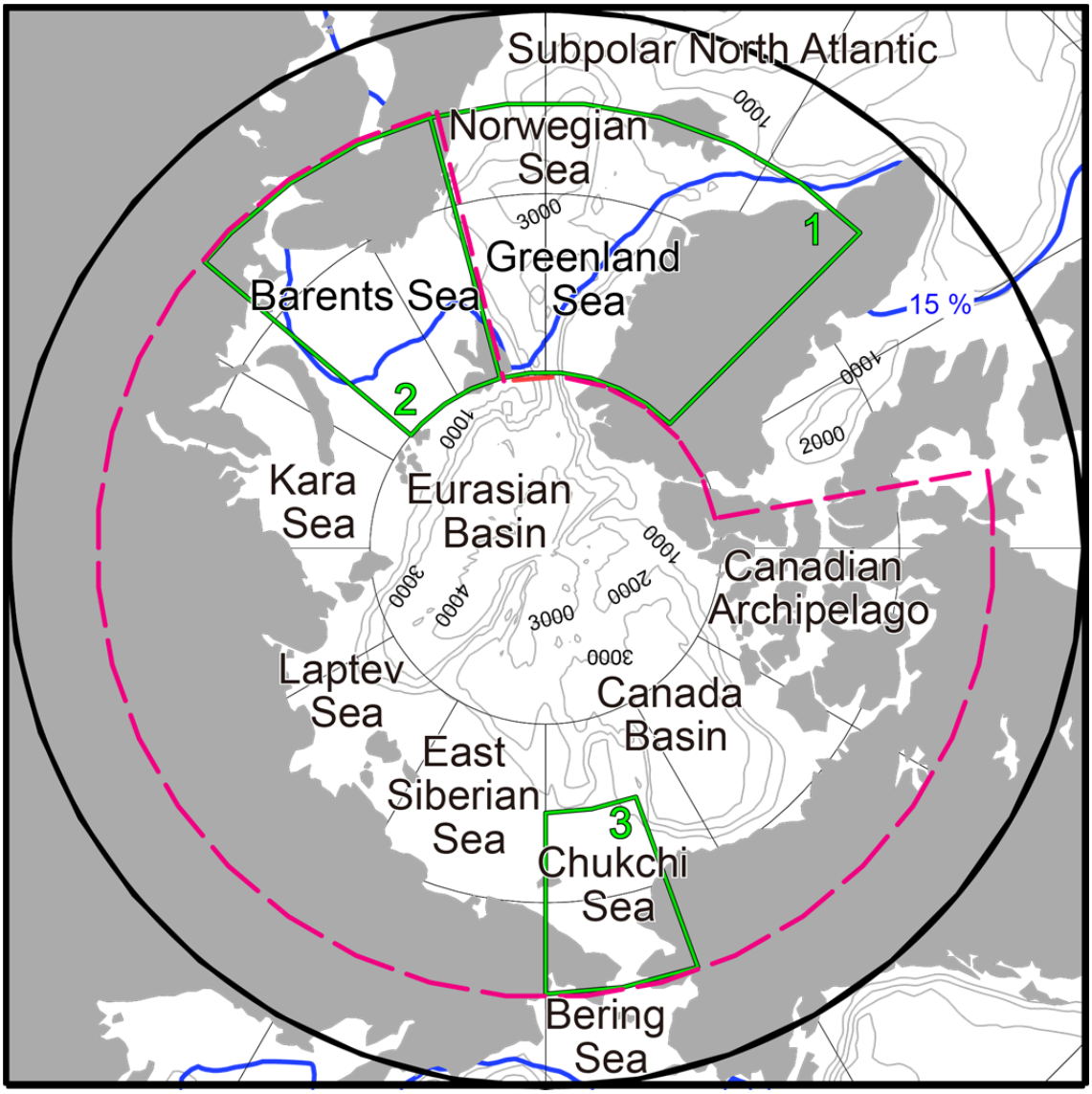

Figure 1: Map of the Arctic Ocean and its adjacent seas. Gray contour lines show the 1000, 2000, 3000, and 4000 m isobaths. Blue lines show the 17-year annual mean position of the ice edge (SIC = 15 %). Area for the mapping is north of 60° N (heavy black circle). Sectors selected for regional analysis are the Arctic Ocean (dashed magenta line), the Greenland/Norwegian Seas (green 1), the Barents Sea (green 2), and the Chukchi Sea (green 3).

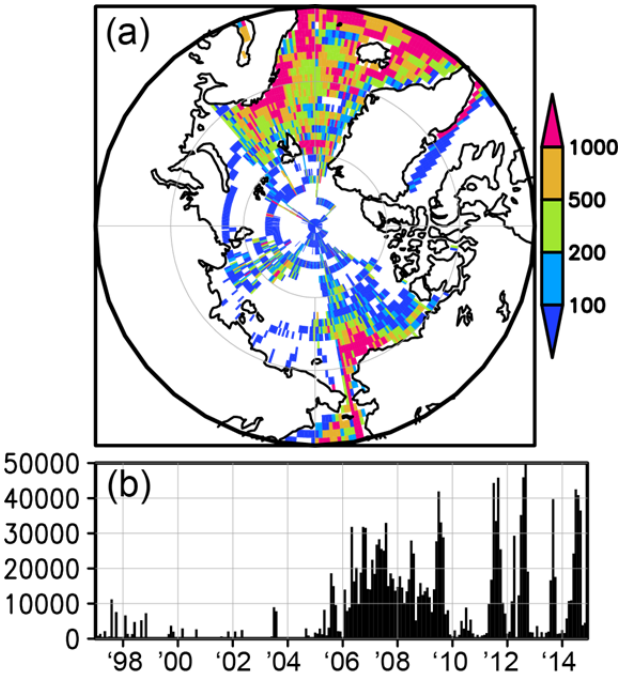

Figure 2: (a) The number of ocean surface CO_2 data in the grid boxes (1° × 1°) used in this study. Data are from SOCATv4, LDEOv2014, GLODAPv2, and collected by R/V *Mirai* of JAMSTEC between 1997 and 2014. (b) Monthly number of CO_2 data in the analysis area (north of 60° N) from 1997 to 2014.

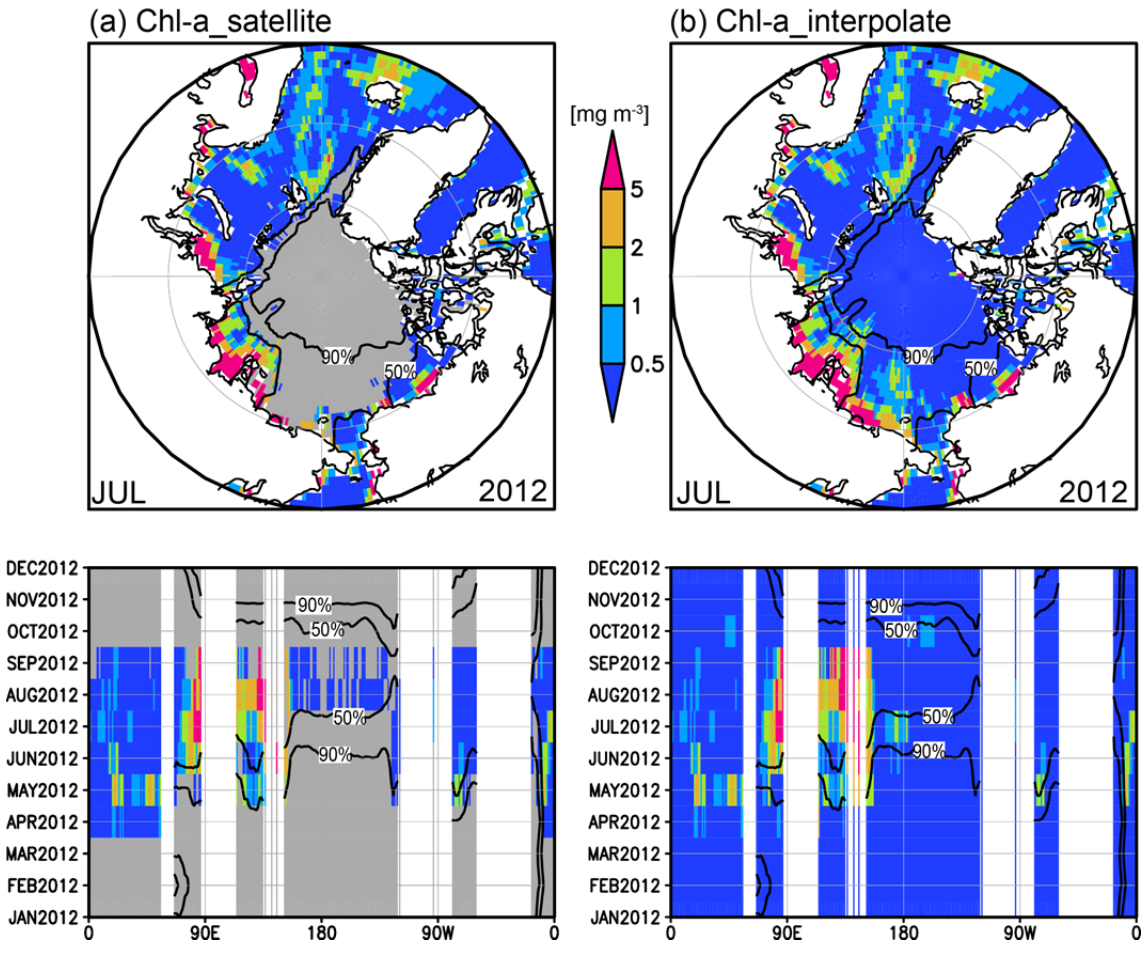

Figure 3: (a) Original and (b) interpolated Chl-a [mg m^{-3}] in July 2012 (upper panels), and along 75°N in 2012 (lower panels). Black lines denote SIC of 50% and 90%. Gray areas in (a) indicate missing Chl-a data.

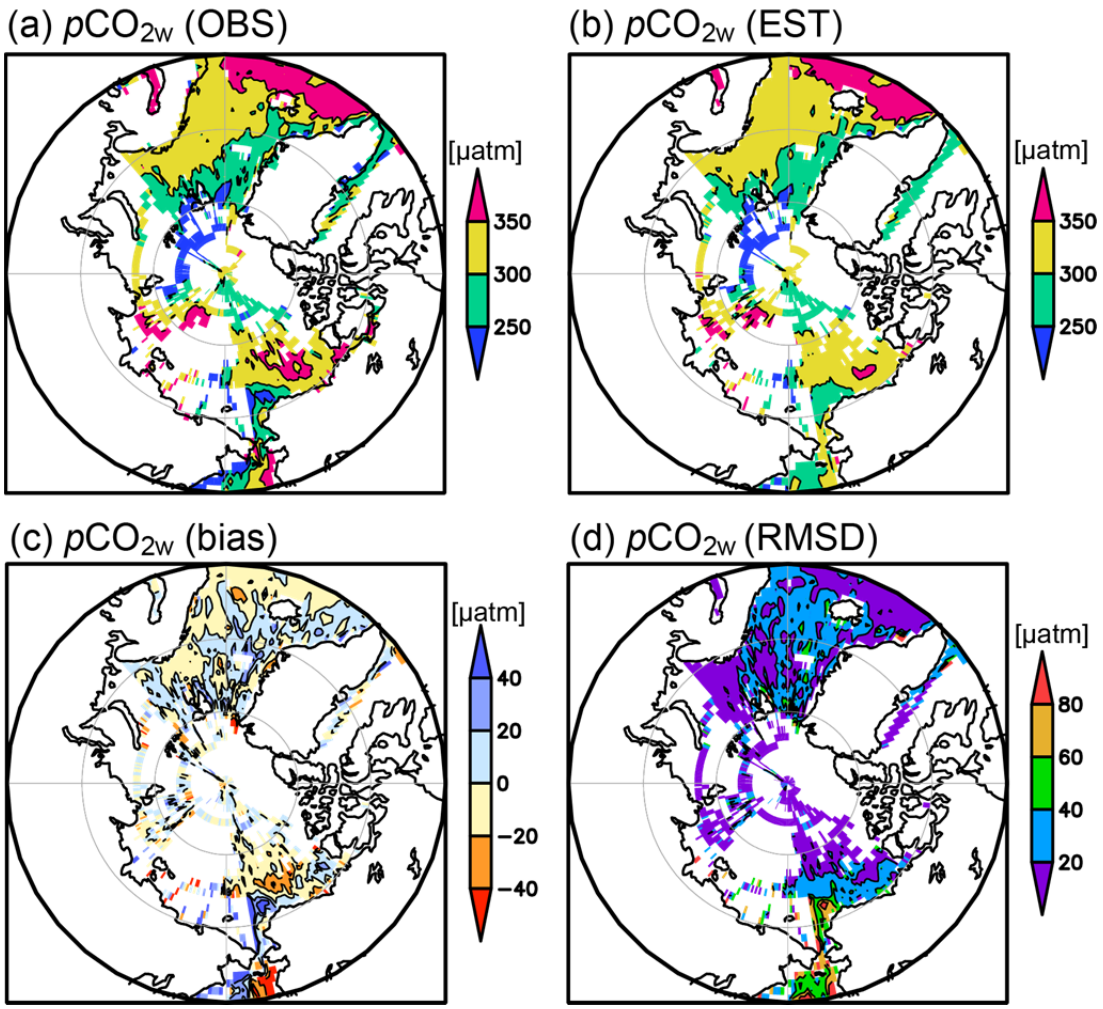

Figure 4: (a) Observed pCO_{2w} averaged over the whole analysis period [µatm]. (b) Estimated pCO_{2w} averaged over the grid boxes in which observed pCO_{2w} values were available [µatm]. (c) Bias (estimate–observation) and (d) root-mean-square-difference between observed and estimated pCO_{2w} averaged over the whole analysis period [µatm].

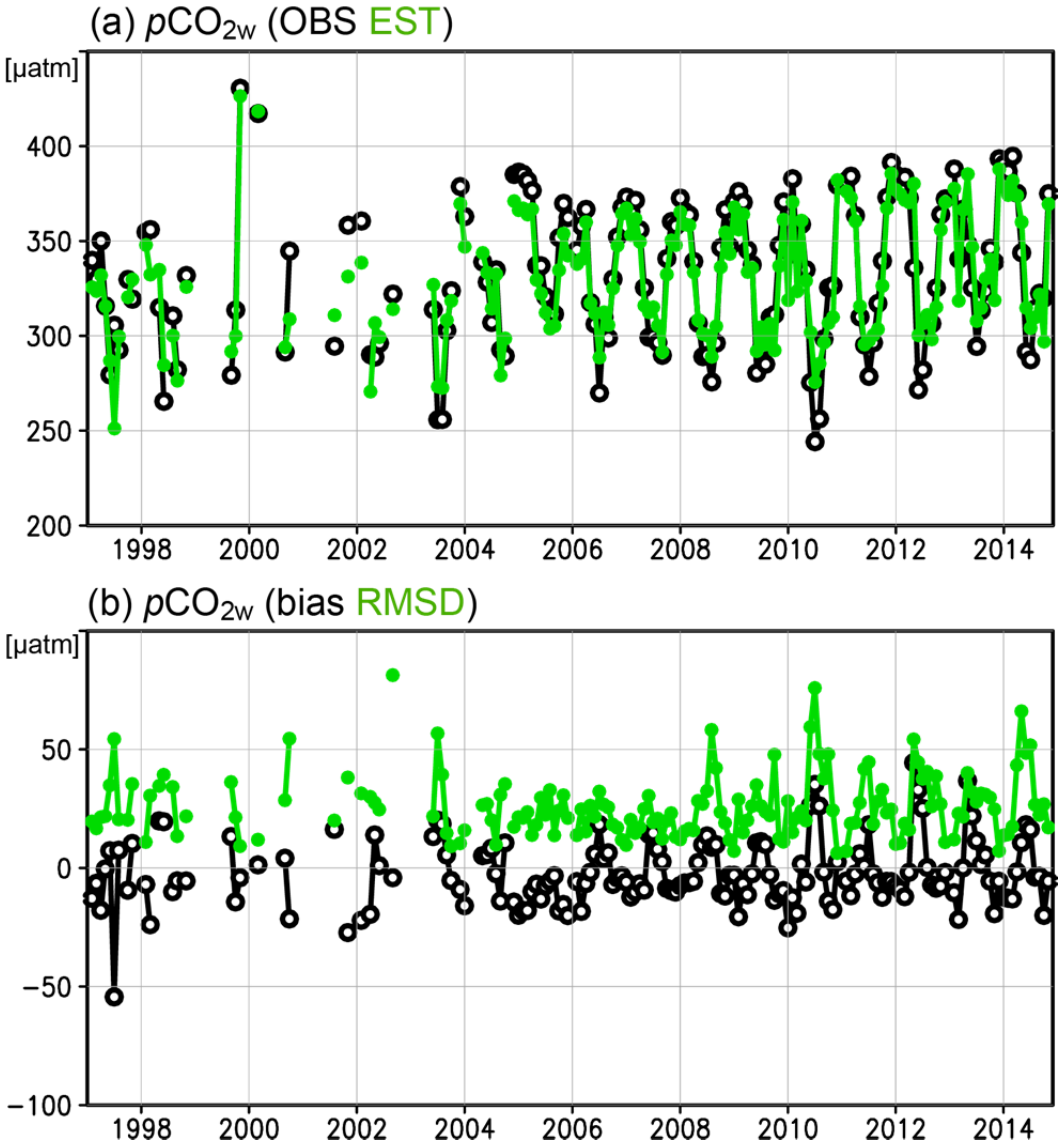

Figure 5: (a) Monthly time series of observed pCO_{2w} averaged over the entire analysis area (black), and estimated pCO_{2w} averaged over the grid boxes in which observed pCO_{2w} values were available (green) [µatm]. (b) Bias (estimate–observation; black) and root-mean-square-difference (green) between observed and estimated pCO_{2w} averaged over the entire analysis area [µatm].

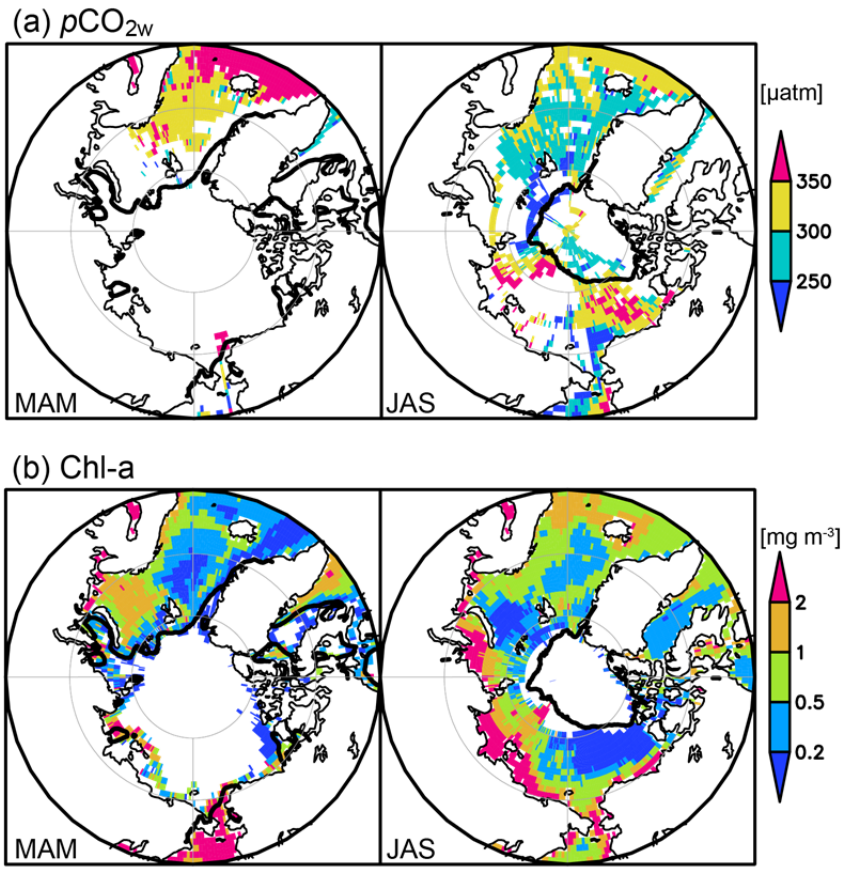

Figure 6: (a) Observed pCO_{2w} [µatm], and (b) non-interpolated Chl-a [mg m^{-3}] in March–May (left), and July–September (right) from 1997 to 2014.

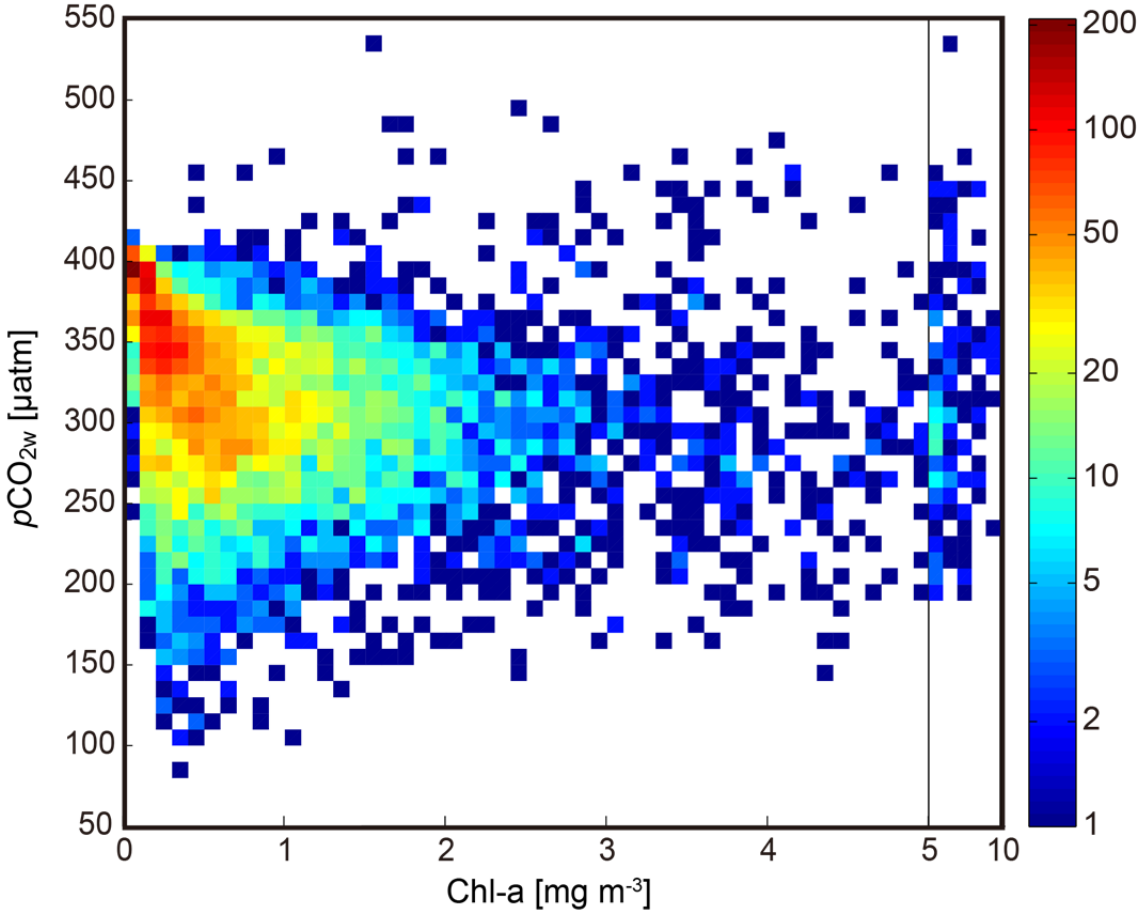

Figure 7: Observed pCO_{2w} [µatm] vs. satellite Chl-a [mg m^{-3}] in the Arctic Ocean and its adjacent seas (north of 60° N) from 1997 to 2014. Colors indicate the number of data pairs in a 0.1 mg m^{-3} × 5 µatm bin when Chl-a ≤ 5 mg m^{-3}, or in a 1 mg m^{-3} × 5 µatm bin when Chl-a > 5 mg m^{-3}.

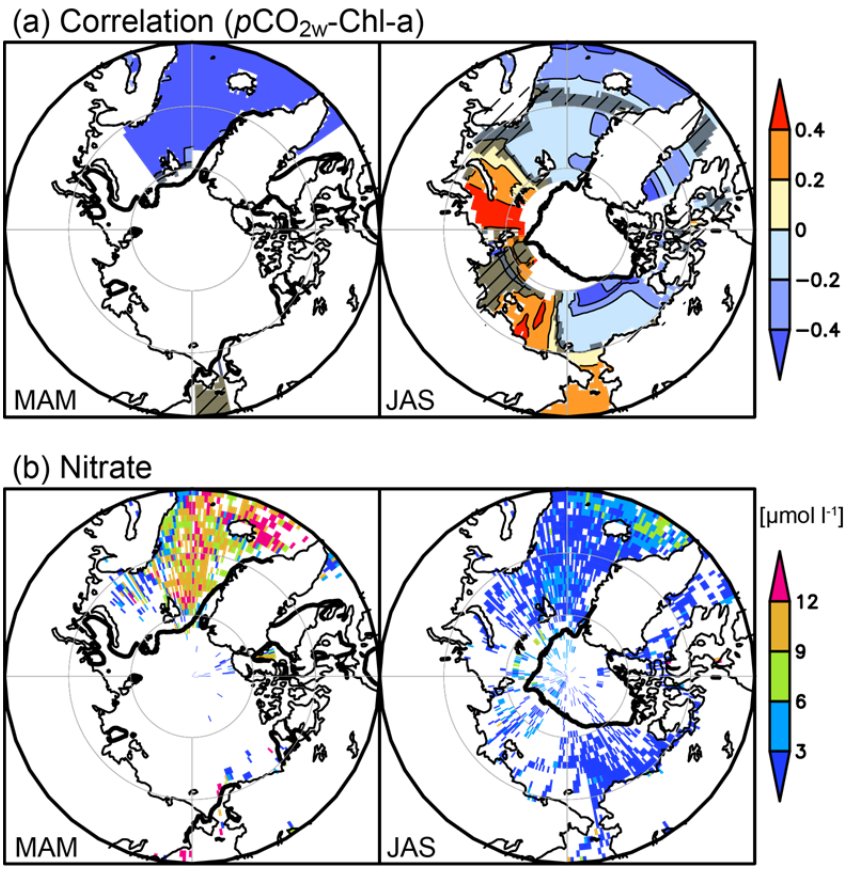

Figure 8: (a) Spatial correlation (correlation coefficient, r) between pCO_{2w} and Chl-a in a window size of ±1 month, ±5° of latitude, and ±30° of longitude in March–May (left), and July–September (right). Darker hatched areas represent values in grids where correlations are insignificant ($P > 0.05$). (b) Surface nitrate concentration [µmol l^{-1}] in March–May (left), and July–September (right) from 1997 to 2014.

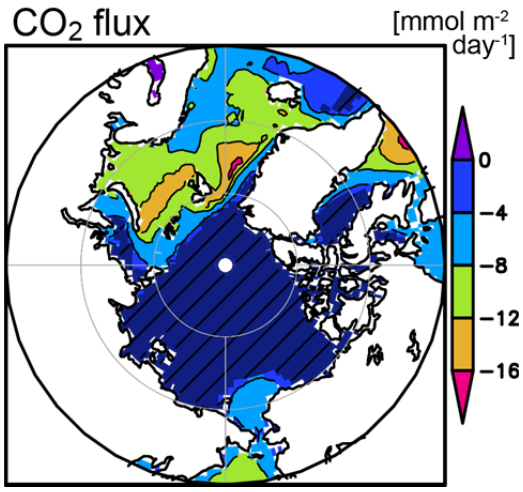

Figure 9: Eighteen-year annual means of CO_2 flux [mmol m^{-2} day^{-1}] (negative values indicate flux into the ocean). Darker hatched areas represent show values in grids where fluxes were smaller than the uncertainty, estimated as described in the text.

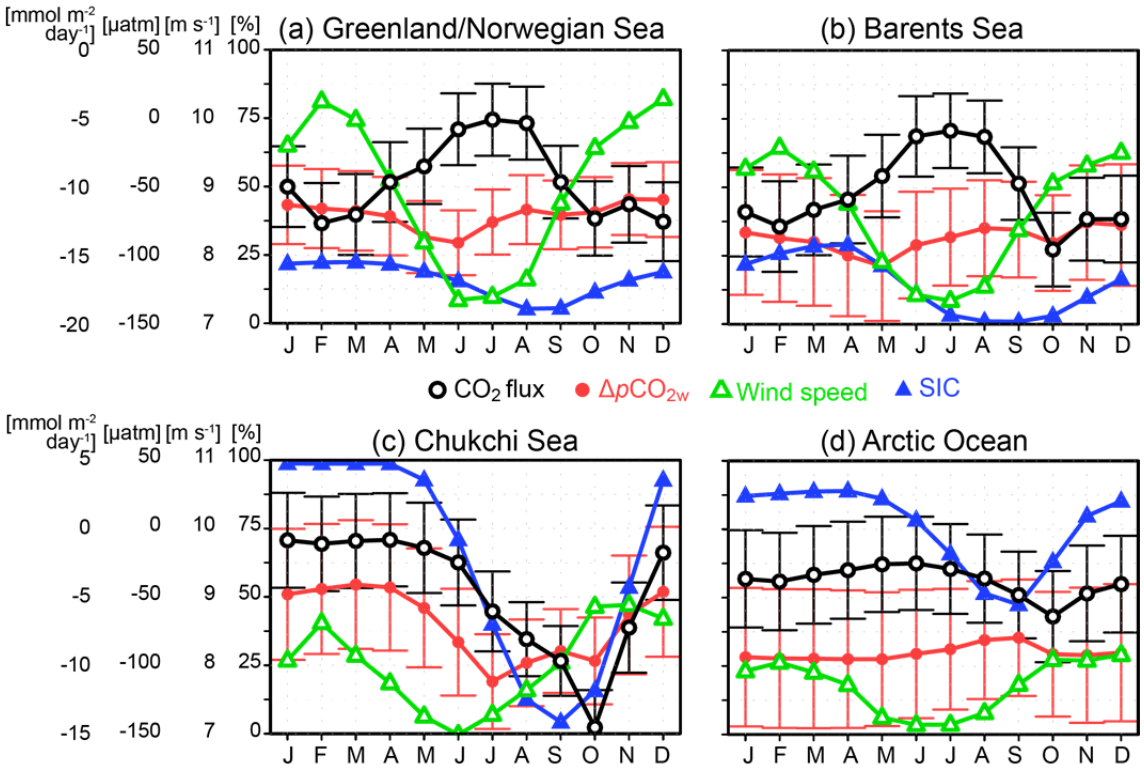

Figure 10: Eighteen-year monthly mean CO_2 flux [mmol m^{-2} day^{-1}] (black), ΔpCO_2 [µatm] (red), wind speed [m sec^{-1}] (green), and SIC [%] (blue), averaged over (a) the Greenland/Norwegian Seas, (b) the Barents Sea, (c) the Chukchi Sea, and (d) the Arctic Ocean. Error bars indicate the uncertainty.

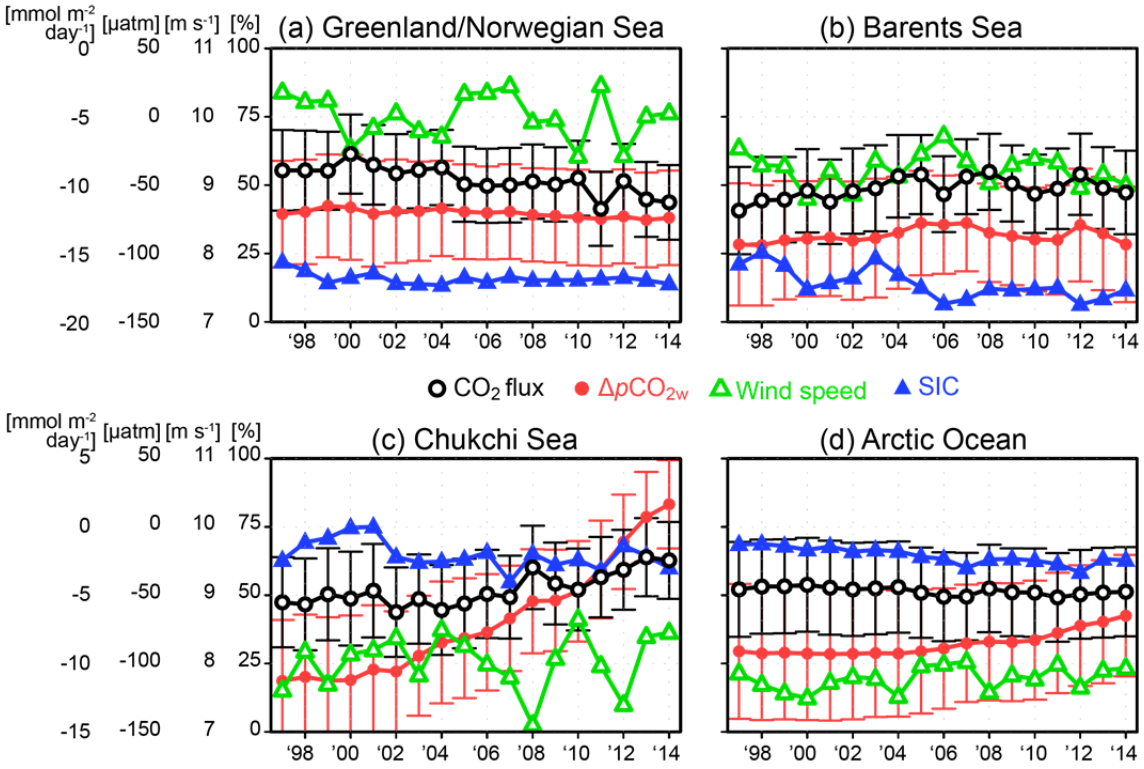

Figure 11: Area-mean interannual variations of CO_2 flux [mmol m^{-2} day^{-1}] (black), ΔpCO_2 [µatm] (red), wind speed [m sec^{-1}] (green), and SIC [%] (blue) in (a) the Greenland/Norwegian Seas, (b) the Barents Sea, (c) the Chukchi Sea, and (d) the Arctic Ocean. Error bars indicate the uncertainty.

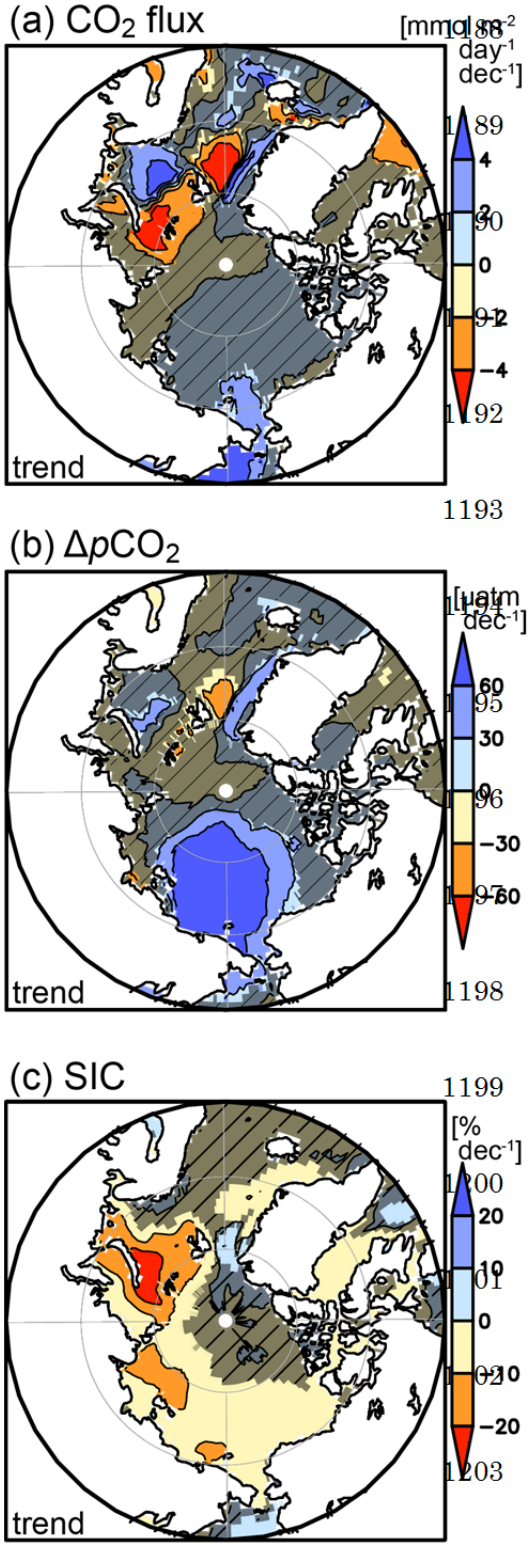

Figure 12: Trends in (a) CO_2 flux [mmol m^{-2} day^{-1} $decade^{-1}$], (b) ΔpCO_2 [µatm $decade^{-1}$], and (c) SIC [% $decade^{-1}$]. Darker hatched areas represent values in grids where trend values were less than the uncertainty, estimated as described in the text.

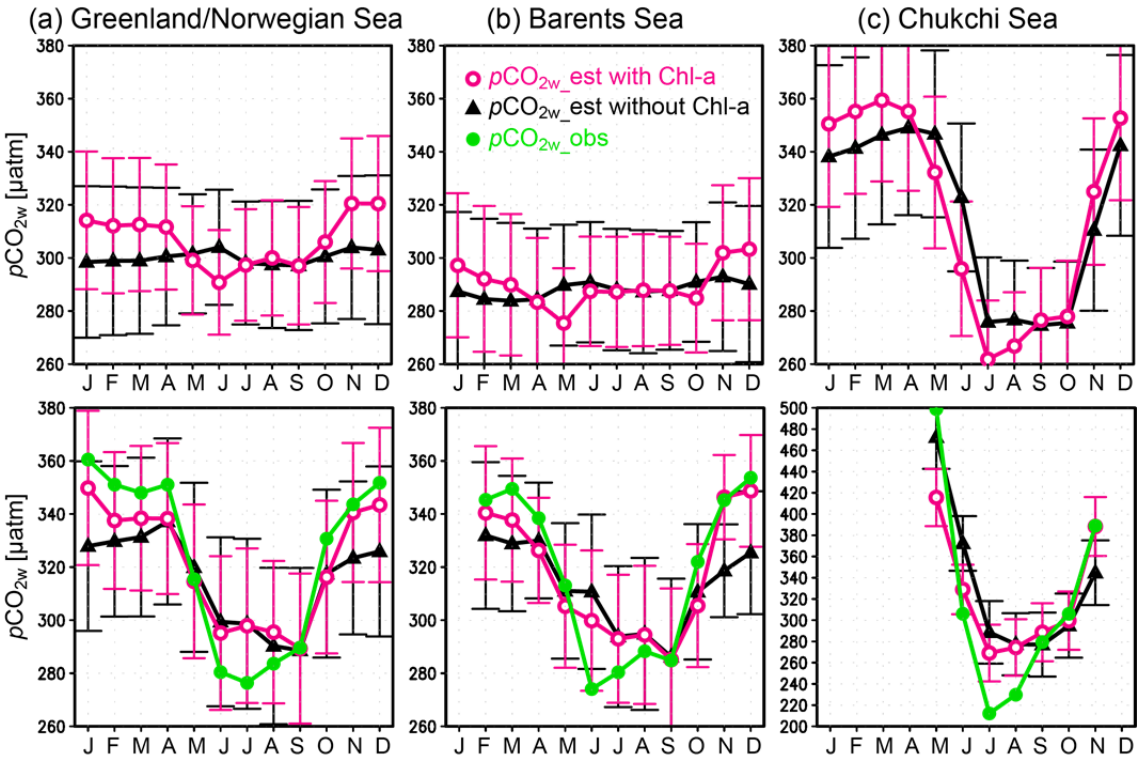

Figure 13: Eighteen-year averaged pCO_{2w} seasonal variations [µatm] in (a) the Greenland/Norwegian Seas, (b) the Barents Sea, and (c) the Chukchi Sea. Black lines with triangles show estimates without Chl-a; magenta lines with open circles show estimates with Chl-a; green lines with closed circles show observed values. The upper panels show pCO_{2w} averaged for all grid cells with each region, and the lower panels show pCO_{2w} averaged over the grid boxes in which observed pCO_{2w} values were available. Error bars show the uncertainty, estimated as described in the text.

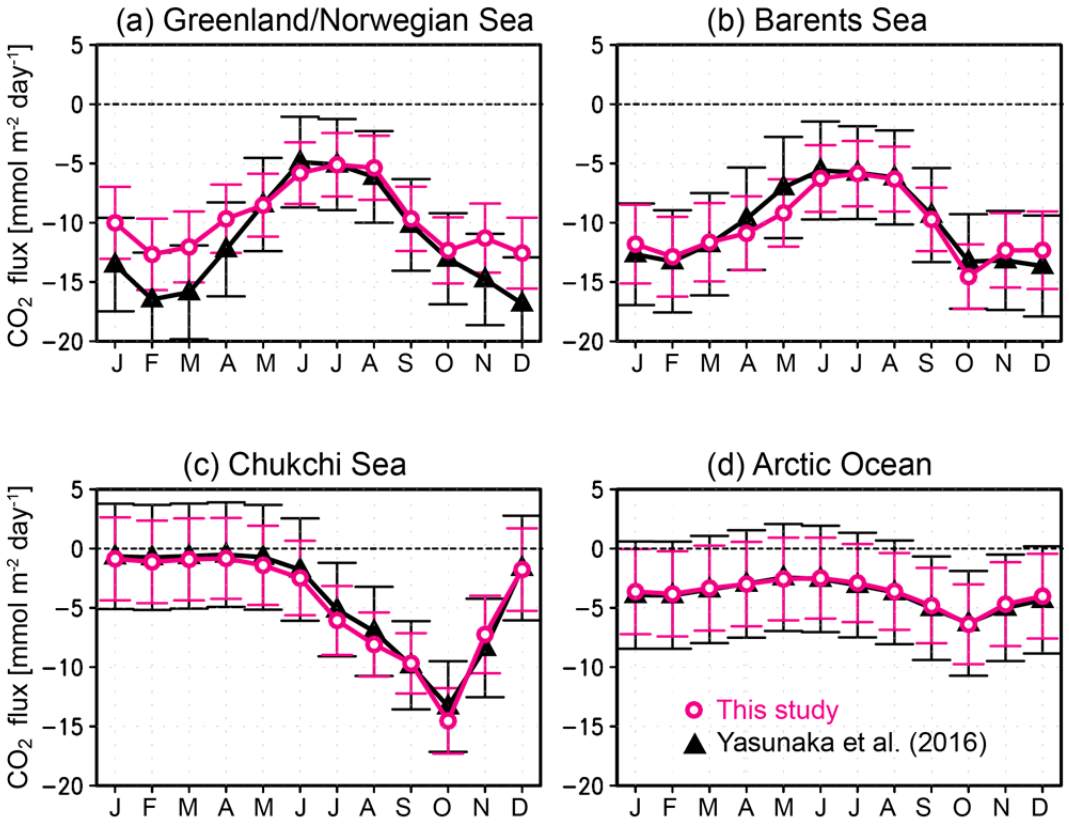

Figure 14: Eighteen-year monthly mean CO_2 flux [mmol m^{-2} day^{-1}] averaged over (a) the Greenland/Norwegian Seas, (b) the Barents Sea, (c) the Chukchi Sea, and (d) the Arctic Ocean. Black lines with triangles show estimates without Chl-a by Yasunaka et al. (2016); magenta lines with open circles show estimates with Chl-a. Error bars show the uncertainty, estimated as described in the text.

1241

1242 Table 1: RMSD [mg m^{-3}] and correlation (r) between Chl-a values

	standard algorithm		coastal algorithm	
	RMSD	r	RMSD	r
Chl-a from Arctic algorithm	0.80	0.90	0.81	0.87
Interpolated Chl-a from Arctic algorithm	0.37	0.92	0.48	0.86

1243

1244

1245